Energy Science & Engineering

WILEY

ORIGINAL ARTICLE OPEN ACCESS

Multiobjective Optimization of Hydrogen-Assisted *Calophyllum inophyllum* Biodiesel Operation in a Compression Ignition Engine

C. Naga Kumar[1] | Nageswara Rao Dayadi[2] | J. M. Babu[3] | Srinivasa Reddy Yarram[4] | Ravikiran Chintalapudi[5] | Bridjesh Pappula[6]

[1]Department of Mechanical Engineering, G. Pullaiah College of Engineering and Technology, Kurnool, Andhra Pradesh, India | [2]Department of Mechanical Engineering, School of Agricultural Engineering and Technology, Kaveri University, Gowraram, Siddipet, Telangana, India | [3]Department of Mechanical Engineering, Vel Tech Rangarajan Dr. Sagunthala R&D Institute of Science and Technology, Avadi, Chennai, Tamil Nadu, India | [4]Department of Mechanical Engineering, PACE Institute of Technology and Sciences (A), Ongole, Andhra Pradesh, India | [5]Department of Mechanical Engineering, MLR Institute of Technology, Hyderabad, Telangana, India | [6]Department of Chemical & Materials Engineering, College of Science, Engineering and Technology, University of South Africa (UNISA), Johannesburg, South Africa

Correspondence: Bridjesh Pappula (epappub@unisa.ac.za)

Received: 1 December 2025 | **Revised:** 16 February 2026 | **Accepted:** 10 March 2026

Keywords: BEMORS | bootstrap bands | *Calophyllum inophyllum* biodiesel | hydrogen | optimization | SMAA

ABSTRACT

This study investigates operating conditions for a diesel engine running in tri-fuel mode with diesel, *Calophyllum inophyllum* biodiesel (0–30 vol%), and inducted hydrogen (0–15 L·min^{-1}) over 0%–100% load (20% steps), yielding 96 steady-state points. Brake thermal efficiency (BTE), brake-specific fuel consumption, exhaust gas temperature, and regulated emissions (NO_x, HC, CO, CO_2, and smoke) were measured. To avoid dependence on a single, fixed objective weighting, Bootstrapped Empirical Multiobjective Ranking and Selection (BEMORS) was applied using percentile scaling, Pareto screening, and Dirichlet preference weights under baseline, NO_x-biased, and NO_x, along with smoke-biased scenarios. Stochastic Multicriteria Acceptability Analysis benchmarking was used to check ranking consistency. Hydrogen enrichment increased BTE and decreased CO, HC, and smoke across loads, while tending to increase NO_x. Increasing biodiesel fraction has also decreased smoke, CO, and HC, but increased fuel consumption due to lower heating value. BEMORS identified 40% load with high hydrogen induction and low biodiesel fraction as the compromise across preference scenarios, whereas high-load hydrogen addition scenarios were attractive when smoke scenarios dominate priorities. Combining tri-fuel experiments with preference-uncertain selection provides practical and implementable operating corridors that are competitive when regulatory emphasis shifts and quantifies the suitability of recommendations within the tested steady-state conditions.

1 | Introduction

Diesel engines face simultaneous constraints from decarbonization targets, air quality regulation, and operational requirements, creating demand for solutions that can be deployed on existing platforms rather than relying on redesign of engine hardware [1]. In this context, alternative and low-carbon fuels are evaluated not only for single metric improvements but for their ability to shift the coupled trade-off among efficiency, NO_x, incomplete combustion products (CO/HC), and soot across realistic load conditions [2, 3]. Biodiesel offers renewable carbon and inherent oxygen content, while hydrogen enrichment provides a high reactivity carbon-free combustion mechanism [4, 5]. However, their combined use typically introduces a more complex NO_x–smoke–efficiency

This is an open access article under the terms of the Creative Commons Attribution License, which permits use, distribution and reproduction in any medium, provided the original work is properly cited.

© 2026 The Author(s). *Energy Science & Engineering* published by Society of Chemical Industry and John Wiley & Sons Ltd.

balance that cannot be resolved by intuition or by reporting a single best operating point.

Calophyllum inophyllum biodiesel (CIB) is a nonedible and high yield with less food versus land competition, which makes it appealing to sustainability and fuel substitution. Reported engine investigations showed that CIB blending tends to decrease smoke, CO, and HC by enhancing better oxidation, whereas CO_2 may increase and act as an indicator of more complete combustion [6, 7]. But brake-specific fuel consumption (BSFC) is increased through the distorted spray/evaporation for CIB, as compared with diesel [8, 9]. The reaction to NO_x is not always universal, and is dependent on the availability of oxygen, injection method, and posttreatment boundary conditions, which have restricted the transferability of any one best blend claim [10, 11]. These trade-offs have been counterbalanced by the use of ignition improvers and oxygenated coadditives (di-*tert*-butyl peroxide, pentanol/butanol, and di-methyl carbonate) that offer the opportunity to improve the quality of ignition and redefine the NO_x soot frontier of CIB blends [8, 11, 12]. Simultaneously, research in processing and pathways of catalysis of *Calophyllum* has minimized production costs, which enables the supply side of CIB implementation at scale [10]. Literature established CIB as a credible decarbonizing agent but also indicates that multipollutant and efficiency goals are not simultaneously satisfied across load using biodiesel blending alone, particularly under fixed engine calibration [12].

Beyond single additive studies, recent studies combine H_2 with biodiesel/diesel and optimize operating ranges using response surface methodology (RSM) and evolutionary/multicriteria decision making (MCDM) or assisted methodologies. Studies have integrated artificial intelligence predictors with RSM to co-optimize brake thermal efficiency (BTE), BSFC, and emissions on biodiesel blends, demonstrating superiority over single-tool optimization [13]. For H_2-enriched biodiesel–diesel dual-fuel diesel engines, multiobjective methods such as RSM, Non-dominated Sorting Genetic Algorithm, Technique for Order Preference by Similarity to Ideal Solution, navigate the efficiency, NO_x, smoke front, and deliver policy-relevant trade-offs [14–16]. Parallel work applied hybrid optimizers to after-treatment (diesel particulate filter capture performance), reinforcing the role of preference-aware optimization in engine fuel codesign [17]. Most multiobjective engine optimization studies proceed in two steps: constructing a Pareto set using RSM surrogates and/or evolutionary solvers and selecting a single implementable operating point using weighted sum desirability, fixed priority constraints, or deterministic MCDM [15]. While effective for identifying trade-offs, these methods typically embed a single, chosen set of weights and a single normalization scheme, implicitly assuming that the preferences are known, stable, and adequate across objectives [16]. In practice, however, fuel blend deployment decisions are made under heterogeneous and shifting priorities, such as NO_x-centric versus smoke-centric regulation, fuel economy versus local air quality constraints, and fleet versus policy viewpoints. Small changes in metric scaling or weight choice can reorder the optimal solutions, particularly when the operating conditions are near the Pareto front.

Although H_2 enrichment with biodiesel has been investigated across several feedstocks, *C. inophyllum* methyl ester is not simply interchangeable with more commonly studied biodiesels because its spray evaporation and operability constraints are more pronounced and can shift the H_2 biodiesel synergy window. CIB has a higher density and viscosity than diesel and may amplify the Sauter mean diameter, promote the wall wetting propensity, and punish low-to-mid load oxidation efficiency unless calibration is reoptimized. Such consequences tend to show themselves in the form of increased BSFC and CO/HC sensitivity in the low-load operation, although smoke is lower in the inherent oxygenation. On the combustion side, CIB biodiesel also forms a clear trade-off geometry with H_2. The high flame speed of hydrogen and high adiabatic temperature, together with the oxygenation, could promote the NO_x risk unless the operating point is chosen judiciously across the load. In this context, H_2 can be used as a reactivity lever to compensate for atomization/evaporation penalties and to recover efficiency, potentially yielding a cleaner multipollutant solution if the engine is operated within an appropriate corridor. On the other hand, most existing approaches report a single optimum rather than quantifying the robustness of operating parameter solutions across reasonable preference scenarios. Decision-making guidance, to vary regulatory emphasis on NO_x and smoke, that treats operating point selection explicitly as a decision problem under preference uncertainty, while also propagating uncertainty from metric scaling/normalization, remains limited in the literature.

This study pursues the following specific objectives:

- Experimentally map performance and emissions for diesel–CIB blends (0–30 vol%) with inducted H_2 (0–15 $L \cdot min^{-1}$) across 0%–100% load, reporting BTE, BSFC, exhaust gas temperature (EGT), NO_x, HC, CO, CO_2, and smoke opacity.
- Quantify load-dependent efficiency emissions trade-offs and identify practically relevant operating corridors for H_2-assisted CIB operation in a compression ignition engine.
- Implement preference-agnostic decision support using Bootstrapped Empirical Multiobjective Ranking and Selection (BEMORS) to identify Pareto-efficient settings, estimate selection probabilities under uncertain preferences, and test robustness under baseline, NO_x-biased, and NO_x with smoke-biased scenarios.
- Benchmark the proposed BEMORS method against Stochastic Multicriteria Acceptability Analysis (SMAA) to validate outcome-level robustness under preference uncertainty and quantify rank acceptability across baseline and emissions-weighting scenarios.

2 | Materials and Methods

2.1 | Fuels and Blend Preparation

Crude *Calophyllum* oil, purchased from a local vendor, was degummed and dried at 60°C under vacuum to remove phosphatides and moisture. Because the feedstock has high free fatty acid, a two-step acid–base transesterification was used. In the acid esterification, the oil was treated with methanol (CAS 67-56-1; purity ≥ 99.9%, Sigma-Aldrich) at a 6:1 molar ratio using 0.8 wt% H_2SO_4 at 60°C under gentle reflux for 60 min, reducing the acid value below 1 wt%. The mixture was allowed to settle, the upper phase was retained, and the base

transesterification followed with fresh methanol at a 6:1 molar ratio and 0.75 wt% potassium hydroxide pellets (CAS 1310-58-3; ≥ 90% purity, Sigma-Aldrich) at 60°C for 60 min under continuous stirring. After ≥ 2 h settled in time, the glycerol layer was decanted. The crude biodiesel was washed with warm deionized water to neutral pH, dried at 60°C under vacuum (for 1 h), and filtered through a 1-μm filtration. Neat fuel was stored in a sealed container at laboratory ambient conditions.

Commercial high-speed diesel was procured from a local vendor and tested against relevant specifications prior to use. Four volumetric diesel fractions were prepared with diesel (100, 90, 80, and 70 vol%) with complementary CIB (0, 10, 20, and 30 vol %) to form binary diesel–biodiesel blends (D100C0, D90C10, D80C20, and D70C30). The target volume of diesel was mixed with the required volume of biodiesel and allowed to mix (20 min at 600 rpm) and left for 12 h to allow the mixture to decant and to check the homogeneity of the phases (no haze/sediment). The batches were filtered through a 5-μm PTFE and a 1-μm glass fiber cartridge into batches. The property measurements were conformed to ASTM procedures and presented in Table 1. The clean CIB met the requirements of the principal D6751 property limits, such as the kinematic viscosity at 40°C ($4.12\ mm^2{\cdot}s^{-1}$ exceeding the D6751 minimum of $1.9–6.0\ mm^2{\cdot}s^{-1}$), flash point (140°C vs. 93°C, D6751 minimum), and cetane number (53 vs. 47, D6751 minimum). The base diesel used in this study is consistent with D975 thresholds for No. 2 diesel, including flash point ≥ 52°C (measured 55.4°C) and viscosity at 40°C within $1.9–4.1\ mm^2{\cdot}s^{-1}$ (measured $2.12\ mm^2{\cdot}s^{-1}$). The blended fuels D90C10–D70C30 retain viscosities of $2.266–2.588\ mm^2{\cdot}s^{-1}$ and flash points of 63.9°C–80.8°C, which remain within/above the corresponding viscosity as per D975 and flash point bounds [11, 12]. This indicated no immediate constraints based on properties for steady-state engine testing under the laboratory conditions. The measured density of neat CIB ($865\ kg\ m^{-3}$) lies within the EN 14,214 band ($860–900\ kg\ m^{-3}$), while diesel ($842\ kg\ m^{-3}$) is within the EN 590 band ($820–845\ kg\ m^{-3}$). Density increases with biodiesel fraction (D90C10–D70C30: $844.3–848.9\ kg\ m^{-3}$), reflecting the higher density of FAME relative to petroleum diesel. All liquid fuels were conditioned to laboratory temperature before tests, and three measurements were taken to ensure repeatability. The photographs of the test fuels are shown in Figure 1.

2.2 | Engine Setup and Procedure

A Kirloskar TV1 single-cylinder, water-cooled diesel engine served as the test platform. The engine was operated at a constant 1500 rpm with a 220-bar fuel injection pressure and a rated brake power of 5.2 kW. An electronic control unit synchronized injector control and crank angle referencing with the in-cylinder pressure transducer, while load was applied using an eddy-current dynamometer (SAJ and AG-20). K-type thermocouples were installed to record temperatures at the air intake, fuel line, coolant outlet, and exhaust manifold. Table 2 lists the full engine specifications. Tests were conducted under 0%, 20%, 40%, 60%, 80%, and 100% load (load indicator: APEX digital, range 0–50 kg, supply 230VAC) using diesel, D90C10, D80C20, and D70C30. Baseline data were acquired on diesel prior to blended fuel trials. The test fuel stock was supplied from a conditioned fuel tank, while high-purity H_2 (≥ 99.995%) was metered into the intake manifold at 0, 5, 10, and 15 $L{\cdot}min^{-1}$ via a dual-stage regulator and mass flow controller (MFC). The H_2 line incorporated check valves and flashback arrestors. A fixed H_2 detector and fail-safe solenoid interlocks shut the supply off on trip or power loss. Leak checks were performed before each experiment. No liquid phase H_2 was used, ensuring that the hydrogen energy fraction (HEF) was controlled independently of the liquid blend composition. Since a constant volumetric flow of H_2 is associated with varying extents of energy substitution with variations in load, addition of H_2 in $L{\cdot}min^{-1}$ was reported along with the inlet HEF on a lower heating value (LHV) basis (Section 2.3).

Combustion diagnostics included in-cylinder pressure (APEX combustion, range 350 bar; diesel line, range 350 bar, with low noise cable) and heat release rate (HRR) derived from pressure-crank angle data (APEX resolution 1°, speed 5500 rpm with top dead center [TDC] pulse). Performance metrics BTE and BSFC were computed from measured fuel use and brake power. Tailpipe emissions (NO_x, CO_2, CO, and HC) and smoke opacity were measured using an AVL DIGAS 444-N five-gas analyzer and an AVL 437 C smoke meter, respectively. All channels were logged with a dedicated data acquisition system (NI USB-6210, 16-bit, 250 kS/s; Engine Soft, Engine performance analysis software). For precision, the engine was run for 15 min, followed by 5–10 min stabilization at each set point. Triplicate measurements were then recorded and averaged. The test schematic is provided in Figure 2. All experiments were

TABLE 1 | The physicochemical properties of test fuels.

Property	*Calophyllum inophyllum* biodiesel	Diesel	D90C10	D80C20	D70C30	ASTM standard
Density @ 15°C ($kg\ m^{-3}$)	865	842	844.3	846.6	848.9	D4052
Cetane number	53	54.5	54.4	54.2	54.0	Derived index
Kinematic viscosity @ 40°C ($mm^2{\cdot}s^{-1}$)	4.12	2.12	2.266	2.421	2.588	D445
Flash point (°C)	140	55.4	63.9	72.3	80.8	D93
Cloud point (°C)	12.2	8	8.4	8.8	9.3	D2500
Pour point (°C)	4.23	6	5.82	5.65	5.47	D97
Calorific value ($kJ{\cdot}kg^{-1}$)	42,497	46,500	46,090	45,682	45,276	D270

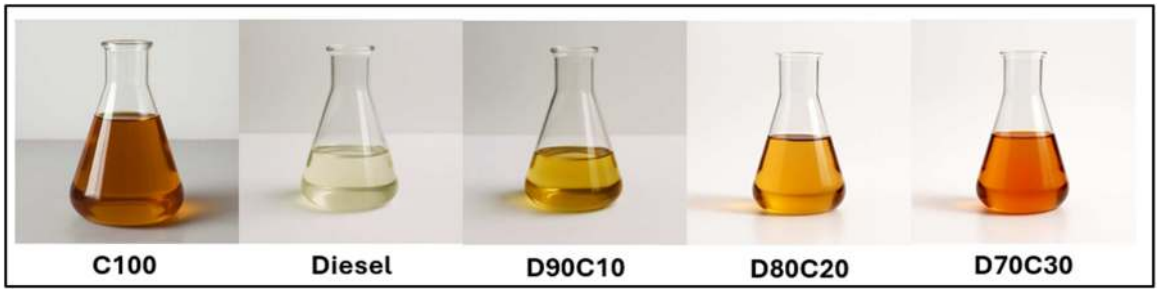


FIGURE 1 | Photographs of test fuels used in the tri-fuel matrix (CIB and diesel blends): C100, diesel, D90C10, D80C20, and D70C30 (vol% diesel:CIB). CIB, *Calophyllum inophyllum* biodiesel.

TABLE 2 | The specifications of the engine.

S. No.	Parameter	Remarks
1	Make and model	Kirloskar, TV1
2	Number of cylinders	1
3	Stroke, mm	110
4	Bore, mm	87.5
5	Piston bowl	Shallow bowl
6	Combustion chamber	Hemispherical
7	Rated power, kW	5.2
8	Compression ratio	17.5:1
9	Fuel injection	Direct injection
10	Rated speed, rpm	1500
11	Number of nozzles	3
12	Fuel injection timing, °CA bTDC	23
13	Fuel injection pressure, MPa	22

Abbreviation: °CA bTDC, crank angle degrees before top dead center.

conducted at 1500 rpm under stabilized steady-state load points (0%–100% load in 20% steps) after thermal and emissions stabilization. The test fuel matrix is shown in Table 3.

Diesel–CIB blends were limited to 0–30 vol% because the resulting viscosities and flash points remain within widely used diesel/biodiesel operational bounds for steady-state testing, avoiding extreme property penalties that can confound attribution of combustion effects. Hydrogen induction levels of 0/5/10/15 $L \cdot min^{-1}$ were chosen as a stepped progression so that it produces a meaningful spread in inlet HEF across loads, enabling interpretation on an energy basis rather than volumetric flow alone. Load was swept from 0% to 100% in 20% steps to represent low-load, midload, and high-load regions, where the H_2–biodiesel interaction is known to change materially due to the load dependence of HEF under fixed SLPM operation.

2.3 | Inlet HEF

The inlet HEF (x_{H_2}) quantifies the share of H_2 in the total fuel energy supplied to the engine on an LHV basis.

$$x_{H_2} = \frac{\dot{Q}_{H_2}}{\dot{Q}_{H_2} + \dot{Q}_{liq}}, \quad 0 \le x_{H_2} \le 1. \tag{1}$$

2.3.1 | Hydrogen Energy Rate

The MFC setpoint is given as a volumetric flow $\dot{V}_{H_2}$ ($L \cdot min^{-1}$) at its reference conditions (P_{ref}, T_{ref}). The MFC setpoint was converted to molar flow via the ideal gas law and then was converted to energy rate using the molar LHV of H_2 as shown in Equation (2).

$$\dot{n}_{H_2} = \frac{\dot{V}_{H_2}}{\bar{V}_m(P_{ref}, T_{ref})} = \dot{V}_{H_2} \times \frac{P_{ref}}{RT_{ref}}, \tag{2}$$

$$\dot{Q}_{H_2} = \dot{n}_{H_2} LHV_{H_2,mol}. \tag{3}$$

For this study, $P_{ref} = 1\,atm$, $T_{ref} = 25°C$, $\bar{V}_m = 24.465\ L \cdot mol^{-1}$, and $LHV_{H_2,mol} = 241.8\ kJ \cdot mol^{-1}$.

2.3.2 | Liquid Fuel Energy Rate

From measured BSFC ($kg \cdot kWh^{-1}$) and brake power P_b (kW), the liquid fuel mass flow is $\dot{m}_{liq} = BSFC \times P_b/3600$ ($kg \cdot s^{-1}$). The liquid energy rate ($\dot{Q}_{liq}$) was estimated using Equation (4).

$$\dot{Q}_{liq} = \dot{m}_{liq} LHV_{blend}. \tag{4}$$

The blend LHV for diesel–CIB was computed on a mass fraction basis using measured densities (ρ) to convert volume fractions (x^V) to mass fractions (w).

$$\text{mass fraction of diesel}, \quad w_d = \frac{x_d^V \rho_d}{x_d^V \rho_d + x_c^V \rho_c},$$

$$\text{mass fraction of } \textit{Calophyllum}, \quad w_c = \frac{x_c^V \rho_c}{x_c^V \rho_c + x_d^V \rho_d},$$

$$\text{LHV of blend}, \quad LHV_{blend} = w_d LHV_d + w_c LHV_c, \tag{5}$$
$$w_d + w_c = 1,$$

The inlet HEF decreases as engine load increases, because the liquid fuel energy rate $\dot{Q}_{liq}$ rises with brake power and BSFC, while $\dot{Q}_{H_2}$ remains constant.

2.4 | Uncertainty Analysis

All reported performance and emissions metrics were accompanied by an uncertainty, combining instrument accuracy,

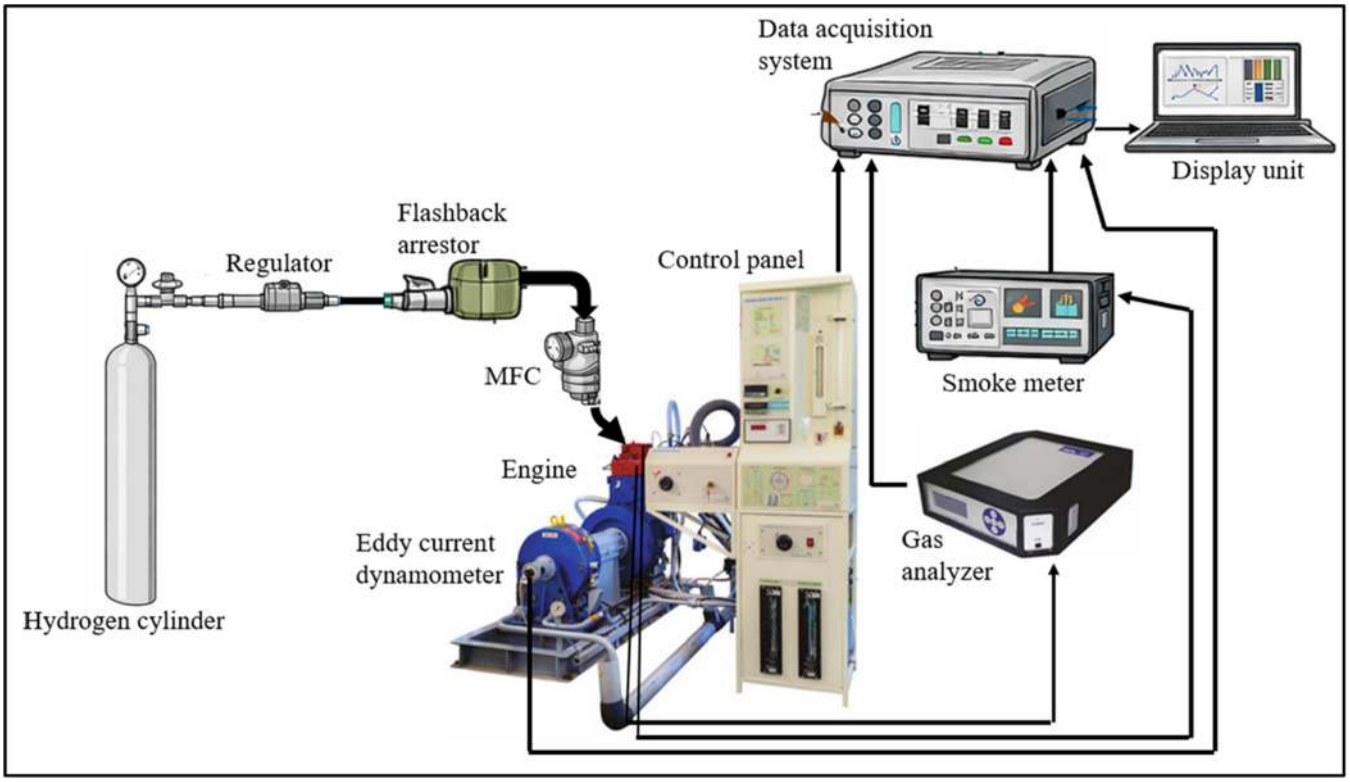


FIGURE 2 | Schematic of the Kirloskar TV1 single-cylinder diesel engine test rig and instrumentation used for tri-fuel experiments: hydrogen cylinder-regulator-flashback arrestor-MFC induction line, eddy-current dynamometer load control, in-cylinder pressure acquisition and DAQ, AVL gas analyzer for NO_x/CO/CO_2/HC, and AVL smoke meter for opacity measurements (tests at constant 1500 rpm; H_2 = 0/5/10/15 L·min^{-1}; load = 0%–100% in 20% steps). MFC, mass flow controller.

TABLE 3 | Test fuel and operating condition matrix (tri-fuel experimental design).

Factor	Remarks
Liquid base fuel blend (diesel:CIB, vol%)	D100C0 (100:0), D90C10 (90:10), D80C20 (80:20), D70C30 (70:30)
Hydrogen induction rate (L·min^{-1})	0, 5, 10, 15
Engine load (%)	0, 20, 40, 60, 80, 100
Total test points	4 blends × 4 H_2 levels × 6 loads = 96 points
Reported responses	BTE, BSFC, EGT, NO_x, HC, CO, CO_2, smoke opacity
Hydrogen energy fraction (%)	Reported per condition (Table S2)

Abbreviations: BSFC, brake-specific fuel consumption; BTE, brake thermal efficiency; CIB, *Calophyllum inophyllum* biodiesel; EGT, exhaust gas temperature.

resolution, and repeatability. Instrument ranges, resolutions, accuracies, and measurement techniques are summarized in Table 4 (CO/CO_2/HC by NDIR, NO_x by electrochemical cell, smoke by opacimeter, speed by magnetic pickup, and EGT by K-type thermocouple), which served as the basis for the analysis.

For a derived measurand $y = f(x_1, ..., x_n)$ (e.g., BSFC, BTE, and emission concentrations), the combined standard uncertainty u_y was obtained by first-order (linear) propagation with sensitivity coefficients $c_i = \partial f / \partial x_i$ as shown in Equation (6).

$$u_y = \sqrt{\sum_{i=1}^{n} (c_i u_{x_i})^2}, \tag{6}$$

where u_{x_i} are the standard uncertainties of the input quantities after converting stated instrument accuracies.

The expanded uncertainty was then reported as $U = k u_y$ with a coverage factor $k = 2$ (approximately 95% confidence) as the degrees of freedom were high and component distributions near normal under steady-state operation. For direct readings (e.g., CO, CO_2, HC, NO_x, smoke, speed, and EGT), u_{x_i} combined the instrument accuracy and resolution from Table 4 with the replicate standard deviation at the same set point. For computed quantities, representative models are shown in Equations (7) and (8).

$$\mathrm{BSFC} = \frac{\dot{m}_f}{P_b} \quad \text{and} \quad \left(\frac{u_{\mathrm{BSFC}}}{\mathrm{BSFC}}\right)^2 = \left(\frac{u_{\dot{m}_f}}{\dot{m}_f}\right)^2 + \left(\frac{u_{P_b}}{P_b}\right)^2, \tag{7}$$

TABLE 4 | The measuring range, resolution, and accuracy of the instruments used.

Measured quantity	Range	Resolution	Accuracy	% Uncertainty	Measurement technique
CO_2	0%–20%	±0.1%	±0.03%	±0.15	NDIR principle
CO	0%–15%	0.001%	±0.02%	±0.02	NDIR principle
NO_x	0–6000 ppm	1 ppm	±5 ppm	±0.05	Electrochemical measurement
HC	0–20,000 ppm	1 ppm	±10 ppm	±0.01	NDIR principle
Speed	0–2000 rpm	5 rpm	±10 rpm	±0.1	Magnetic pickup type
Smoke	0%–100%	0.1%	±1%	±1	Opacimeter
EGT	0°C–1000°C	±1°C	±1°C	±1.5	K-type thermocouple

Abbreviations: EGT, exhaust gas temperature; NDIR, nondispersive infrared.

$$\mathrm{BTE} = \frac{P_b}{\dot{m}_f \mathrm{LHV}} \quad \text{and} \quad \left(\frac{u_{\mathrm{BTE}}}{\mathrm{BTE}}\right)^2 = \left(\frac{u_{P_b}}{P_b}\right)^2 + \left(\frac{u_{\dot{m}_f}}{\dot{m}_f}\right)^2 + \left(\frac{u_{\mathrm{LHV}}}{\mathrm{LHV}}\right)^2, \tag{8}$$

here, $u_{\dot{m}_f}$ reflects the volumetric-to-mass conversion using density, and u_{P_b} combines dynamometer torque and speed uncertainties.

All channels were recorded under steady-state conditions using a synchronized data acquisition system and stabilized operation. Applying this methodology, an overall uncertainty was 2.31% for the principal reported metrics, consistent with the instrument specifications in Table 4.

2.5 | Multiobjective Optimization and Robust Selection

To identify operating points that balance efficiency and emissions without presupposing a single trade-off, a BEMORS procedure was applied to the 96-run data set, presented as Table S1. In the BEMORS method, each metric was mapped to a unit interval using percentile scaling (5th–95th) and direction unification, yielding a comparable score vector for every operating point. A Pareto screening step isolates the nondominated parameter set and computes dominance-gap diagnostics. Preference uncertainty was then modeled through Dirichlet distribution utility weights, from which Monte Carlo sampling produces selection probabilities for each sample. These probabilities quantify the frequency with which a setting emerges as optimal across probable trade-offs, rather than under a single fixed weight vector. Finally, robustness is tested via (i) Dirichlet concentration sweeps (preference sharpness) and policy skewed prior (e.g., NO_x or NO_x + smoke scenarios), and (ii) bootstrap resampling of the normalization step to generate stability bands on selection probabilities. The outputs are decision-grade operating recommendations supported by probability ranks, uncertainty bands, and geometric diagnostics. The overview of the BEMORS workflow used for robust multiobjective operating point selection is shown in Figure 3.

2.5.1 | *Problem Statement and Notation*

Let $i \in \{1, \ldots, N\}$ denote the number of experiments ($N = 96$). Let the objectives be BTE, CO_2, BSFC, EGT, NO_x, HC, CO, and Smoke. Define the direction vector $d = (+, +, -, -, -, -, -, -)$, where "+" denotes the maximize and "−" denotes the minimize. For each metric m, with raw values y_{im}, the robust unit interval score $x_{im} \in [0,1]$ is constructed so that higher is better for all objectives. Denote the set of "maximize" indices by M_+ and "minimize" indices by M_-. In this study, CO_2 is not treated as an environmental benefit in the conventional greenhouse gas accounting sense. Instead, under the steady-state, fixed-speed experimental boundary, CO_2 is used as a completeness combustion proxy that helps discriminate operating points where reductions in CO/HC (and smoke) arise from improved oxidation rather than from incomplete burning. Thus, CO_2 is only represented as a benefit-type criterion in the normalized decision space to ensure the internal consistency of the completeness signal among the candidate points. On the basis of this, CO_2 is only mapped as a benefit-type criterion in the normalized decision space to impose internal consistency of the completeness signal with candidate points. This study does not prove that increased CO_2 is inherently good, and it does not place CO_2 as a mitigation objective of climate.

2.5.2 | *Robust Scaling and Direction Unification*

To reduce outlier influence, scores are computed using quantile (5th–95th) min–max scaling, as shown in Equation (9).

$$\tilde{x}_{im} = \frac{y_{im} - Q_{0.05}(m)}{Q_{0.95}(m) - Q_{0.05}(m)} \quad \text{clipped to } [0,1]. \tag{9}$$

Direction is unified by inversion for minimize-type metrics, as shown in Equation (10).

$$x_{im} = \begin{cases} \tilde{x}_{im}, & m \in M_+, \\ 1 - \tilde{x}_{im}, & m \in M_-. \end{cases} \tag{10}$$

Let $x_i = (x_{i1}, \ldots, x_{iM})^T$ with $M = 8$.

2.5.3 | *Pareto Analysis*

A setting j dominates j (denoted $j \succ i$), as shown in Equation (11), if

$$x_{jm} > x_{im} \quad \forall\, m \text{ and } \quad \exists\, m : x_{jm} > x_{im}. \tag{11}$$

The Pareto set P consists of all nondominated i. P in the scaled space $[0,1]^M$ was computed.

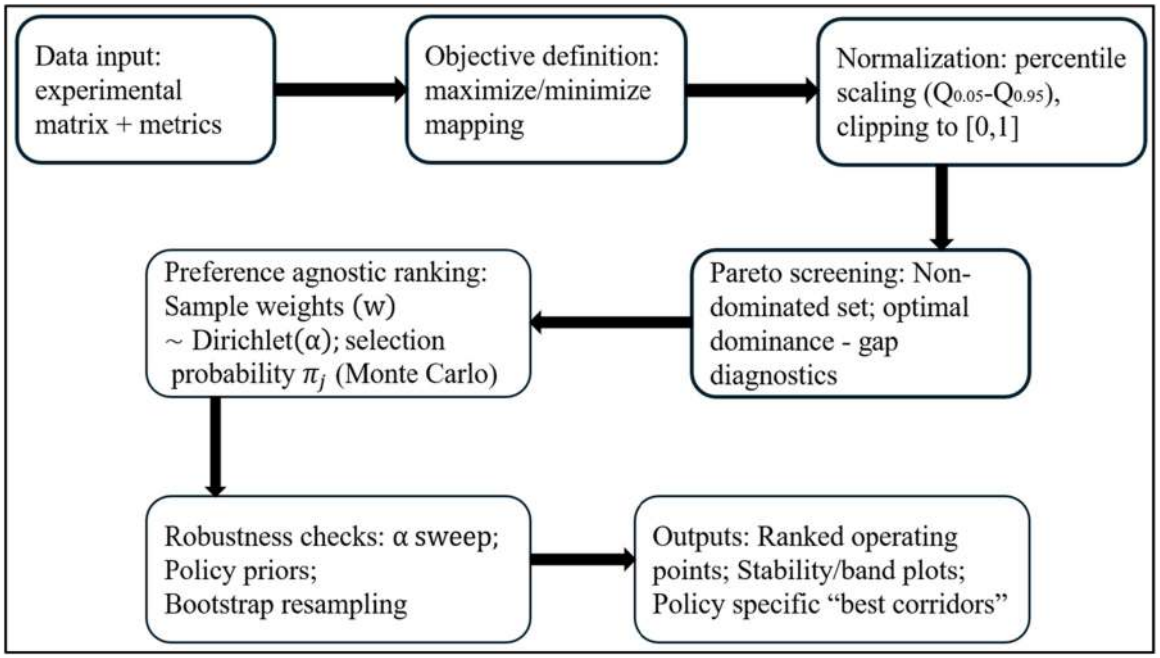


FIGURE 3 | Overview of the BEMORS optimization and robust selection workflow applied to the 96-point tri-fuel data set: objective mapping, quantile scaling/clipping, Pareto screening, preference-uncertain ranking (Dirichlet sampled weights), robustness checks, and policy-relevant outputs. BEMORS, Bootstrapped Empirical Multiobjective Ranking and Selection.

2.5.3.1 | *Dominance Gap*

For any i, define the dominance gap (g_i) under the L_∞ gauge, as shown in Equation (12).

$$g_i = \begin{cases} 0, & i \in P, \\ \max\limits_{j:j>i} \max\limits_{m}, & i \notin P. \end{cases} \tag{12}$$

Larger g_i indicates the greater potential improvement to reach the front.

2.5.3.2 | *Hypervolume (HV)*

With reference point 0 (since scores are in $[0, 1]$), the HV of P is shown in Equation (13).

$$\mathrm{HV}(P) = \lambda(\{z \in [0,1]^M : \exists\, p \in P \ \text{s.t.}\ p \geq z\}), \tag{13}$$

where λ is the Lebesgue measure. HV is estimated via Monte Carlo sampling over $[0,1]^M$.

2.5.4 | *Preference-Agnostic Selection via BEMORS*

The unknown stakeholder trade-offs by random utility weights $w = (w_1, \ldots, w_M)^T$ on the probability simplex is shown in Equation (14).

$$w \sim \mathrm{Dirichlet}(\alpha), \quad w_m \geq 0, \quad \sum_m w_m = 1. \tag{14}$$

Given w, the score of experiment i is $S_i(w) = w^T x_i$. The winner for that draw is estimated using Equation (15) with ties shared equally.

$$A(w) = \arg\max_i S_i(w). \tag{15}$$

The selection probability of experiment i under prior α is shown in Equation (16).

$$p_i(\alpha) = \Pr_{w \sim \mathrm{Dir}(\alpha)}(A(w) = i). \tag{16}$$

2.5.4.1 | *Monte Carlo Estimator and CI*

With R i.i.d. draws $\{w^{(r)}\}_{r=1}^R$,

$$\hat{p}_i = \frac{1}{R}\sum_{r=1}^{R} I(A(w^{(r)}) = i) \tag{17}$$

and a binomial Wilson 95% interval is shown in Equation (18).

$$\mathrm{CI}_{0.95}(\hat{p}_i) = \frac{\hat{p}_i + \frac{z^2}{2R} \pm z\sqrt{\frac{\hat{p}_i(1-\hat{p}_i)}{R} + \frac{z^2}{4R^2}}}{1 + \frac{z^2}{R}}, \quad z = 1.96. \tag{18}$$

2.5.4.2 | *Prior Sensitivity*

Robustness is probed to preference sharpness by $\alpha = c \cdot 1$ with $c \in \{0.2, 0.5, 1, 2, 5\}$. Small c emphasizes spiky preferences (near single metric). Large c emphasizes averaging preferences.

2.5.4.3 | *Policy Scenarios (Asymmetric Priors)*

Regulatory emphasis is encoded by asymmetric α. For instance,

$$\alpha_{\mathrm{NO}_x} = 2, \quad \alpha_{m \neq \mathrm{NO}_x} = 1 \Rightarrow w \sim \mathrm{Dirichlet}(\alpha)$$

upweights NO_x in the distribution of utility vectors without fixing a single weight vector. Analogous settings are used for NO_x + Smoke.

2.5.5 | *Bootstrap Stability*

Because scores depend on empirical quantiles, the stability was assessed by bootstrapping the data set used to compute $Q_{0.05}$ and $Q_{0.95}$. For $b = 1, \ldots, B$, resample the N rows with replacement, recompute quantile scalers and obtain bootstrapped scores x_i^{*b}, and re-estimate $\hat{p}_i^{*b}$ with a moderate R. The bootstrap mean and 2.5%–97.5% quantiles of $\{\hat{p}_i^{*b}\}$ provide stability bands arising from the scaling step.

2.5.6 | *Assumptions and Safeguards*

Scale invariance: Robust percentile scaling ensures objectives are commensurate and mitigates tail leverage.

Preference uncertainty: Instead of prescribing a single weight vector, the Dirichlet prior integrates across plausible trade-offs.

Uncertainty decomposition: Wilson CIs quantify Monte Carlo variability, bootstrap bands capture uncertainty from scaling (data-driven quantiles).

Policy relevance: Asymmetric priors emulate regulatory emphasis without collapsing the problem to a single criterion.

2.6 | Benchmarking Using SMAA

To be compared with the proven techniques of preference-uncertain MCDM, an SMAA was run as a benchmark. SMAA is uniquely applicable in decision situations in which the preferences of the decision makers are known or unknown. In SMAA, every candidate operating point is assessed under a collection of likely weight vectors, and the result is summarized by way of rank acceptability indices [18]. The benchmarking process is defined as targeted external validation with the aim of establishing the credibility and reproducibility of the observed probabilistic ranking behavior, as based upon the established stochastic MCDM baseline.

2.6.1 | *Criteria Matrix and Robust Score Construction*

The SMAA analysis was based on the same experimental design matrix and eight criteria that are employed during the optimization workflow. To make the process of fairness and straightforward comparability with BEMORS, the raw criteria were converted into a single benefit-oriented score space. All criteria were scaled to 5th–95th percentile and then scaled to $[0, 1]$ and the directionality was normalized such that high values always represent improvement. Specifically, BTE and CO_2 were mapped as benefit-type criteria, whereas BSFC, EGT, NO_x, HC, CO, and smoke were mapped as cost-type criteria and inverted after scaling. CO_2 is included only as a complete proxy under fixed operating points, not as a climate objective. It is interpreted jointly with CO/HC to avoid conflating lower CO_2 concentration with environmental benefit. This produced a normalized score matrix $S \in [0,1]^{N \times M}$ (with N candidate operating points and $M = 8$ criteria) that can be consumed consistently by both SMAA and BEMORS.

2.6.2 | *Preference-Uncertainty Model and Utility Evaluation*

Preference uncertainty was represented by sampling weight vectors w from the probability simplex using a Dirichlet distribution, $w \sim \mathrm{Dirichlet}(\alpha)$, which is used for modeling uncertain trade-offs while ensuring nonnegativity and unit sum constraints. The baseline scenario used the non-informative setting $\alpha = 1$, which corresponds to uniform sampling of admissible weight vectors. In addition, two policy priors were evaluated to reflect sustainability decision contexts, that is, NO_x upweighted preferences, and NO_x + smoke upweighted preferences, consistent with the probabilistic decision analysis. For each sampled w, a scalar utility was computed using Equation (19) and alternatives were ranked in descending order of U_i.

$$U_i(w) = \sum_{j=1}^{M} w_j S_{ij}. \tag{19}$$

This Monte Carlo procedure was repeated at a large sample size to stabilize acceptability estimates.

2.6.3 | *Rank Acceptability and Summary Indicators*

SMAA summarizes preference-uncertain performance using rank acceptability indices, defined as the probability that a candidate achieves a given rank across the sampled preference space [19]. Let $b_i^{(r)}$ denote the rank acceptability of alternative i at rank r. The analysis reports (i) the Rank 1 acceptability $b_i^{(1)}$ (best sample), (ii) cumulative acceptability such as $P(\text{top-3}) = \sum_{r=1}^{3} b_i^{(r)}$ and $P(\text{top-5})$, and (iii) the expected rank $\mathbb{E}\mathrm{rank}_i$, which provides a stability-aware measure beyond a single winner-takes-all selection. These indicators are particularly useful for engine fuel optimization because multiple operating points can be near equivalent in deterministic score space yet diverge substantially once preference perturbations are admitted.

2.6.4 | *Benchmark Agreement Criteria and Scope*

SMAA is used as a benchmark for preference-uncertainty behavior, not as an independent validation of the experimental measurements. To avoid confirmatory interpretation, agreement between SMAA and BEMORS is evaluated using predefined concordance indicators computed under matched priors and the same normalized criteria matrix. Agreement is defined at three levels: (i) Winner stability, the BEMORS Rank 1 configuration remains within the SMAA top-k set with nontrivial probability mass, (ii) Leader-set overlap between the top-5 sets produced by SMAA and by BEMORS probability ranking, and (iii) Global ranking consistency, that is, correlation between BEMORS selection probabilities and SMAA rank-1 acceptability across all candidate operating points. Robustness is claimed only when winner stability holds across the baseline and policy. When leader-set overlap is sustained, recognizing that rank dispersion is expected under heterogeneous stakeholder trade-offs.

3 | Results and Discussion

To interpret combustion trends under a fixed H_2 volumetric flow, it is necessary to account for the inlet HEF. Since the inducted H_2 energy rate is constant for a given $L \cdot min^{-1}$ while the liquid fuel energy rate increases with load, HEF decreases as load rises. Accordingly, changes in premixed heat release, pressure rise behavior, and NO_x formation with H_2 are expected to be most pronounced at operating points with higher HEF (typically low-to-mid load for a fixed $L \cdot min^{-1}$). A high load would have the same $L \cdot min^{-1}$ translated into a smaller energy fraction and potentially reduced or later phased effects. This HEF scaling offers the quantitative foundation of correlating the measured in-cylinder pressure/HRR shifts and emissions responses to H_2 contribution. The total increased uncertainty on a comparative change was about ±3.3%. Thus, in the results, percentage changes that are less than 3.3% have been treated as being marginal and possibly within experimental error, and they should not be treated as mechanistic. Conversely, alterations of more than 3.3% are understood to be quantifiable and strong within the boundaries of error in the experiment. The conclusion of all CO_2-related statements is reported in a conservative manner and with a combination of CO/HC patterns, and the discussion of the results is done in a way that little CO_2 changes close to the measurement uncertainty are treated as inconclusive. This will make sure that the trends in performance and emissions reported are looked at with the necessary statistical caution and conclusions made, focusing on the effects that can clearly be identified in comparison to the experimental uncertainty.

3.1 | In-Cylinder Pressure Analysis

Figure 4 illustrates the variation of in-cylinder pressure at 100% load of the diesel and the diesel–CIB–H_2 blends. H_2 enrichment at constant base fuel increased the peak pressure relative to neat diesel (P_{max} = 60.03 MPa at 10°aTDC). D100C0H15 exhibited 65.43 MPa at 12°aTDC. CIB blends contain a smaller yet constant uplift (D70C30H0: 61.83 MPa). The combination has the maximum effect in D70C30H15 (67.39 MPa) and D80C20H15 (68.50 MPa) has shown the highest in-cylinder pressure. These tendencies are consistent with the modern evidence of the fact that small H_2 shares increase the premixed burn fraction and sharpen the initial heat release, in turn, increasing P_{max} at full load [6, 7]. With a fixed H_2 inlet, the replacement of diesel by CIB (10–30 vol%) has a slight effect on peak cylinder pressure (diesel to D70C30H0 was +3% at full load).

Given the reported combined uncertainty of the principal metrics (2.31%) and the cycle-to-cycle variability inherent to steady-state pressure acquisition, this is interpreted as a weak

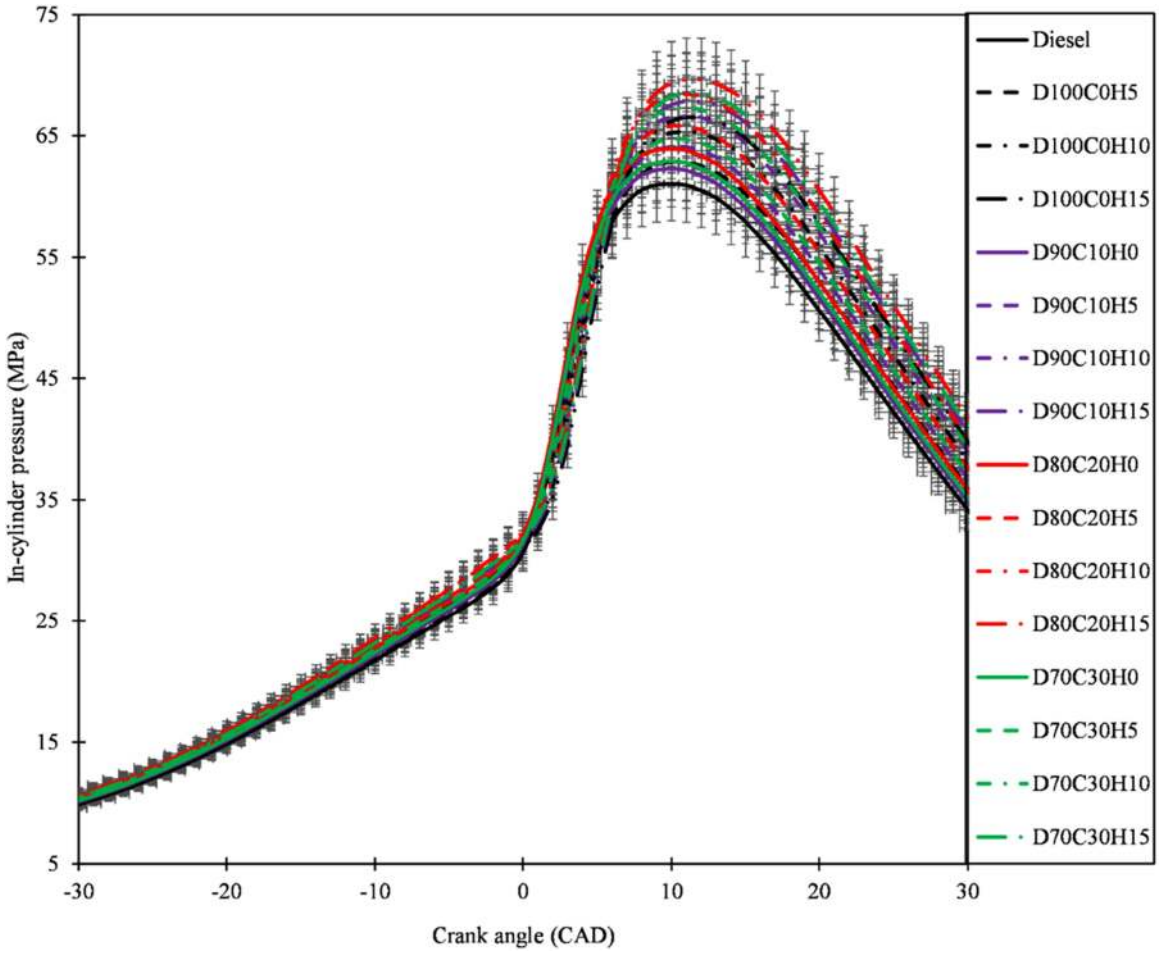


FIGURE 4 | In-cylinder pressure traces at 100% load for diesel and diesel–CIB blends (D100C0, D90C10, D80C20, D70C30) under hydrogen induction rates H0/H5/H10/H15 at constant 1500 rpm. CIB, *Calophyllum inophyllum* biodiesel.

but directionally consistent tendency rather than a decisive change in combustion severity. Accordingly, mechanistic attribution is restricted to a qualitative level (oxygenation-related changes in diffusion burning), while the dominant and clearly resolvable effect remains the larger pressure rise associated with H_2 enrichment. This behavior is consistent with oxygenated fuels, where local equivalence ratios are lowered near the spray, flame luminosity and late diffusion burning are suppressed, and the premixed burn fraction is enhanced [20]. Effects reported for CIB in recent engine studies show that the biodiesel oxygenation supports modest P_{max}, faster early burning [21–23]. The high laminar flame speed and low quenching distance in H_2 amplify the premixed burn fraction and the initial heat release increase, which raises P_{max} at high load [24, 25]. Higher cetane for many biodiesels (feedstock dependent on *Calophyllum*) supports cleaner diffusion burning and slightly higher P_{max} at the same load [20]. The highest P_{max} occurs when oxygenated liquid fuel is mixed with moderate H_2 (15 L·min^{-1}), a configuration emphasized in studies on H_2-enriched biofuels that report enhanced premixed burning and improved pressure/HRR dynamics [7].

Because H_2 was metered as a fixed volumetric flow rate (5–15 L·min^{-1}), its effective contribution to the total chemical energy input varies substantially with load and blend composition. Accordingly, pressure-trace trends were interpreted using the inlet HEF reported in Table S2. Across the experimental matrix, HEF spans 2.19%–25.69%, reaching its maximum at low-load/high H_2 conditions (e.g., diesel, 15 L·min^{-1}, 20% load, 25.69%) and decreasing systematically as load increases because the liquid fuel energy rate increases while the inducted H_2 energy rate remains fixed. At 100% load, HEF remains materially nonzero but is markedly lower than at part load and is blend dependent. For diesel, HEF for diesel was found to be 3.74/7.56/11.45% at 5/10/15 L·min^{-1}. For D90C10, it was 3.13/6.37/9.72%. For D80C20, it was 2.62/5.36/8.23%, and for D70C30, it was 2.19/4.50/6.94%. Therefore, changes in the premixed burn intensity, peak pressure timing, and rate-of-pressure-rise behavior driven by H_2 at full load should be interpreted as effects occurring under a moderate HEF band. Whereas stronger sensitivity to H_2 at low-to-mid loads is consistent with substantially higher HEF levels at the same L·min^{-1}.

3.2 | Heat Release Rate

The HRR variations for the test fuels at 100% load are presented in Figure 5. Relative to neat diesel ($\dot{Q}_{max} = 39.61$ J·deg^{-1} at 2°CA), H_2 enrichment steepens the early burn and raises peak HRR. At D100C0H15, $\dot{Q}_{max}$ rises to 49.43 J·deg^{-1} (+24.8% vs. diesel) and CA shifts later to 6.29°. The start of combustion (SOC) shifts from −6°CA to −4°CA, indicating an earlier onset relative to TDC despite the later CA. Blends with both CIB and H_2 maintain this intensification. D70C30H15 exhibited +20.3% in $\dot{Q}_{max}$ with CA50 + 2.62° later than diesel, and D80C20H15 reached +21.7% with CA50 + 2.24°. With 30 vol% CIB and no

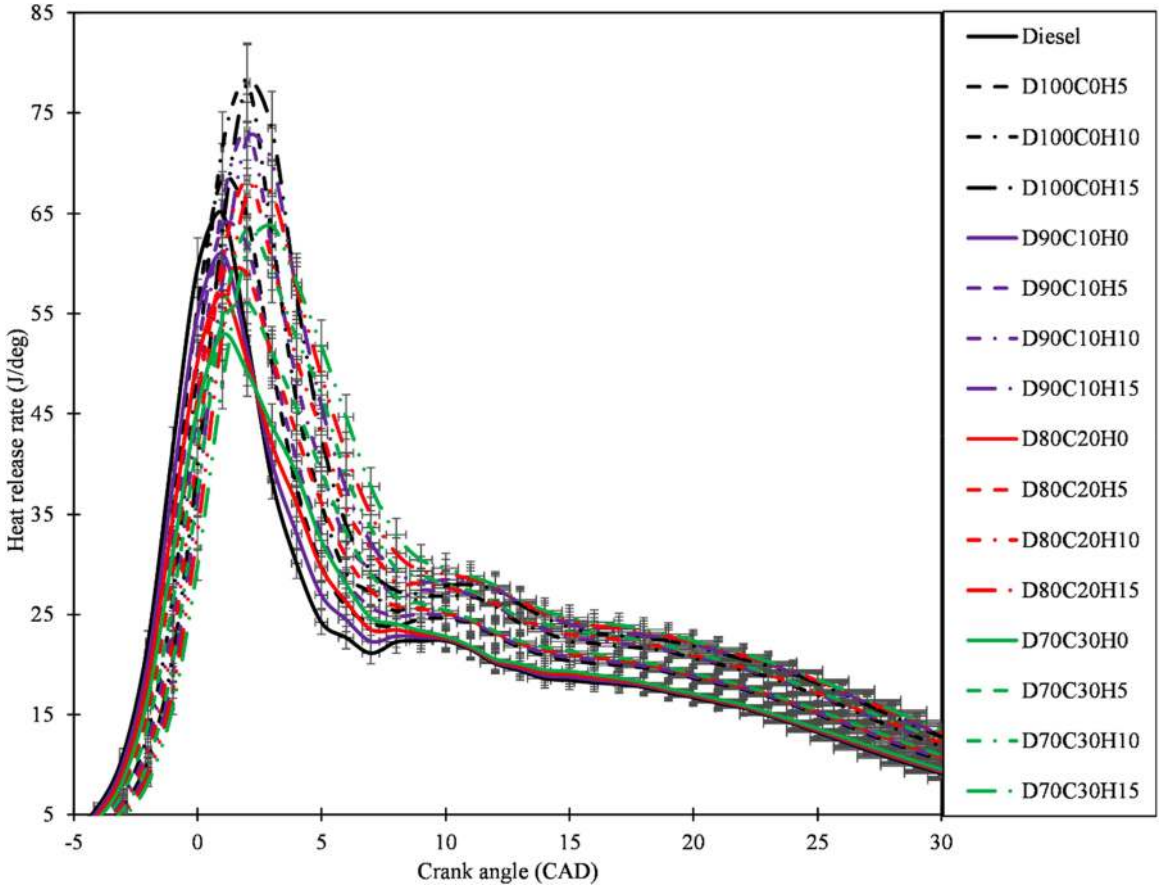


FIGURE 5 | Net heat release rates at 100% load for diesel and diesel–CIB blends (D100C0, D90C10, D80C20, and D70C30) under hydrogen induction rates H0/H5/H10/H15 at constant 1500 rpm. CIB, *Calophyllum inophyllum* biodiesel.

H_2 (D70C30H0), the peak HRR differs only slightly from diesel (−2.75% at full load), while CA50 shifts modestly (+1.10°).

The overall uncertainty (2.31%), the 1°CA resolution of the acquisition, and the extra sensitivity of apparent HRR to derivative processing pressure have to be taken into consideration. This slight change in HRR is close to the experimental/processing margin. Thus, the biodiesel effect at full load is addressed as a reshaping of the heat release profile, as opposed to a statistically significant decrease in peak HRR. Whereas the H_2 cases exhibited an intensification (+20%–25%) which crosses across the band of uncertainty. Such a slight decrease in peak HRR is in line with the finding that biodiesels are more likely to reduce peak HRR due to increased viscosity and decreased LHV [20]. Yeneneh et al. reported a linear decline in peak HRR as the share of biodiesel increased and a recovery of HRR at full load with preheating [26].

In hydrogenated cases, the SOC threshold (10% of peak HRR crossing near TDC) was also advanced by 1°–2° and CA50 was also delayed by 1.5°–2.6° compared with diesel. This combination begins sooner, but a CA50 has shifted into expansion, which agrees with a greater premixed increase preceded by primary burning under full load. Such behavior is supported by recent dual-fuel analyses, which have higher early chemistry rates with H_2 and enhanced early mixing, and injector/jet interaction effects that adjust, in which the bulk heat has evolved [27]. H_2–diesel blend configurations (or small interaction angles) can advance heat release and increase pressure rise, whereas other angles lengthen combustion and reshape the CA50 window. In contrast, CIB alone slightly reduces $\dot{Q}_{max}$ but can improve oxidation later in the cycle, lowering smoke at the expense of some efficiency, a trend widely reported for oxygenated biodiesels [26, 28]. The combined biodiesel and H_2 effect shows that H_2 largely overcomes the biodiesel-only HRR penalty, while keeping the benefits of oxygenation, an outcome of dual-fuel studies pairing H_2 with oxygenated fuels [2, 5, 6].

The heat release response to H_2 addition could be interpreted in terms of the HEF rather than volumetric flow alone, because a fixed H_2 flow rate corresponds to widely different energetic substitutions across loads. Table S2 shows that HEF spans 2.19%–25.69% across the test matrix, with the highest values occurring at low load (e.g., diesel at 20% load: 9.40/17.93/25.69% for 5/10/15 $L{\cdot}min^{-1}$) and progressively decreasing at higher loads due to the rising liquid fuel energy rate. Consequently, the HRR at 100% load occurred under a lower HEF regime than at part load. At 100% load, HEF was 3.74%–11.45% for diesel, 3.13%–9.72% for D90C10, 2.62%–8.23% for D80C20, and 2.19%–6.94% for D70C30 (for 5–15 $L{\cdot}min^{-1}$). At low-to-mid loads, the influence of H_2 can be amplified by higher HEF, whereas at high loads, the same $L{\cdot}min^{-1}$ corresponds to a smaller energetic share and therefore modifies the HRR primarily through kinetic/transport effects (high diffusivity and flame speed) rather than through large energy substitution.

3.3 | Brake Thermal Efficiency

The variations in BTE for all test fuels are presented in Figure 6. Hydrogen consistently increases BTE at all loads for diesel fuel. Relative to neat diesel, BTE increased from 34.12% to 36.82% at 100% load with H_2 at 15 $L{\cdot}min^{-1}$ (7.9%). At 100% load, D70C30H0 demonstrated 24.40% versus diesel 34.12%. Hydrogen partially restores biodiesel BTE, with recovery increasing with H_2 rate. For 30% biodiesel, 24.40% (0 $L{\cdot}min^{-1}$) to 29.25% (15 $L{\cdot}min^{-1}$) at 100% load (19.9%). Ranking at full load is D100C0H15 (36.82%) > D100C0H10 (35.86%) > D100C0H5 (34.72%) > diesel (34.12%) > D90C10H15 (32.42%) > D80C20H15 (31.12%) > D70C30H15 (29.25%).

The drop in BTE for biodiesel can be attributed to lower LHV and altered spray breakup/evaporation. During phase retuning, more fuel energy is required per kWh, and controlled diffusion burning can persist for longer [29, 30]. In the case of biodiesel and H_2, the initial chemistry of H_2 is faster and the greater LHV penalty is compensated, and the diffusion burning is alleviated. The effect of H_2 on BTE is positive, which is in correspondence with modern dual-fuel evidence. This demonstrates that small, metered doses of H_2 increase the release of premixed heat and decrease incomplete combustion losses, particularly at the medium and high loads [4, 5].

The proportion of HEF is 2.19%–25.69% over the operating matrix as a whole and has an inverse linear proportionality to load at a constant H_2 setpoint. The liquid fuel energy rate is proportional to brake power, and the inducted H_2 energy rate is relatively limited. In all blends, BTE improved with the increase of HEF at a fixed load, and this implies that the efficiency advantage is determined by the H_2 energy share instead of the absolute flow rate [13]. To illustrate this, when the HEF was raised to 11.45% (diesel + H_2) at full load, BTE increased to 36.82% rather than the 34.72% when the HEF was raised to 3.74%. In the case of D90C10H5, HEF increased by 3.13%–9.72% and BTE increased by 27.64%–32.41%. In the case of D80C20H5, the HEF increased by 2.62%–8.23% and BTE increased by 26.53%–31.12%. In the case of D70C30H5, HEF increased by 2.19%–6.94% and BTE increased by 24.94%–29.25%. This is consistent with H_2 compensating for the higher viscosity/lower LHV penalties of biodiesel operation by strengthening the early premixed burn and promoting more complete oxidation [31]. An elevated HEF augments the ratio of a premixed, highly reactive H_2–air charge, which elevates flame propagation capacity and the prompt release of heat following pilot ignition. This tends to shorten the viable combustion time and enhance more phasing toward the thermodynamic efficiency. Recent H_2–diesel dual-fuel studies similarly emphasized that efficiency results are best interpreted against energy fraction/substitution level, because the same metered H_2 can correspond to materially different energetic participation depending on load and air path conditions [24].

3.4 | Brake-specific Fuel Consumption

The variations in BSFC for all test fuels are presented in Figure 7. H_2 consistently reduced BSFC for neat diesel, with larger gains at higher load. Diesel: 0.341–0.284 $kg{\cdot}kWh^{-1}$ at 100% load with 15 $L{\cdot}min^{-1}$ H_2 (16.7% improvement), at 80% load 0.354–0.299 (15.5% improvement), at 60% load 0.381–0.332 (12.9% improvement), and at 40% load 0.442–0.386 (12.7% improvement). H_2 offsets 15%–17% of that penalty at full load. D90C10: 0.413–0.345 with 15 $L{\cdot}min^{-1}$ (16.5% improvement). D80C20: 0.501–0.418 (16.6% improvement). D70C30: 0.607–0.506 (16.7% improvement). Despite recovery, absolute

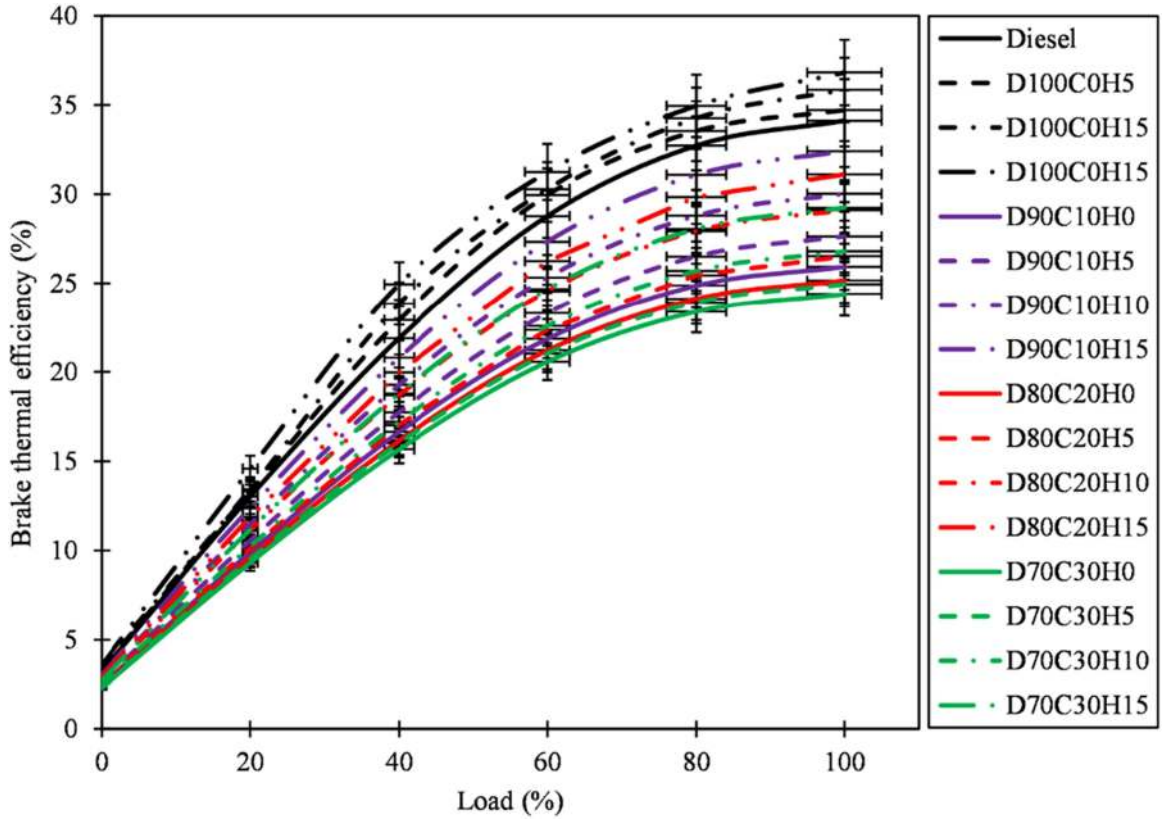


FIGURE 6 | Brake thermal efficiency versus load (0%–100% in 20% steps) for diesel and diesel–CIB blends under hydrogen induction 0/5/10/15 L·min^{-1} at constant 1500 rpm speed. CIB, *Calophyllum inophyllum* biodiesel.

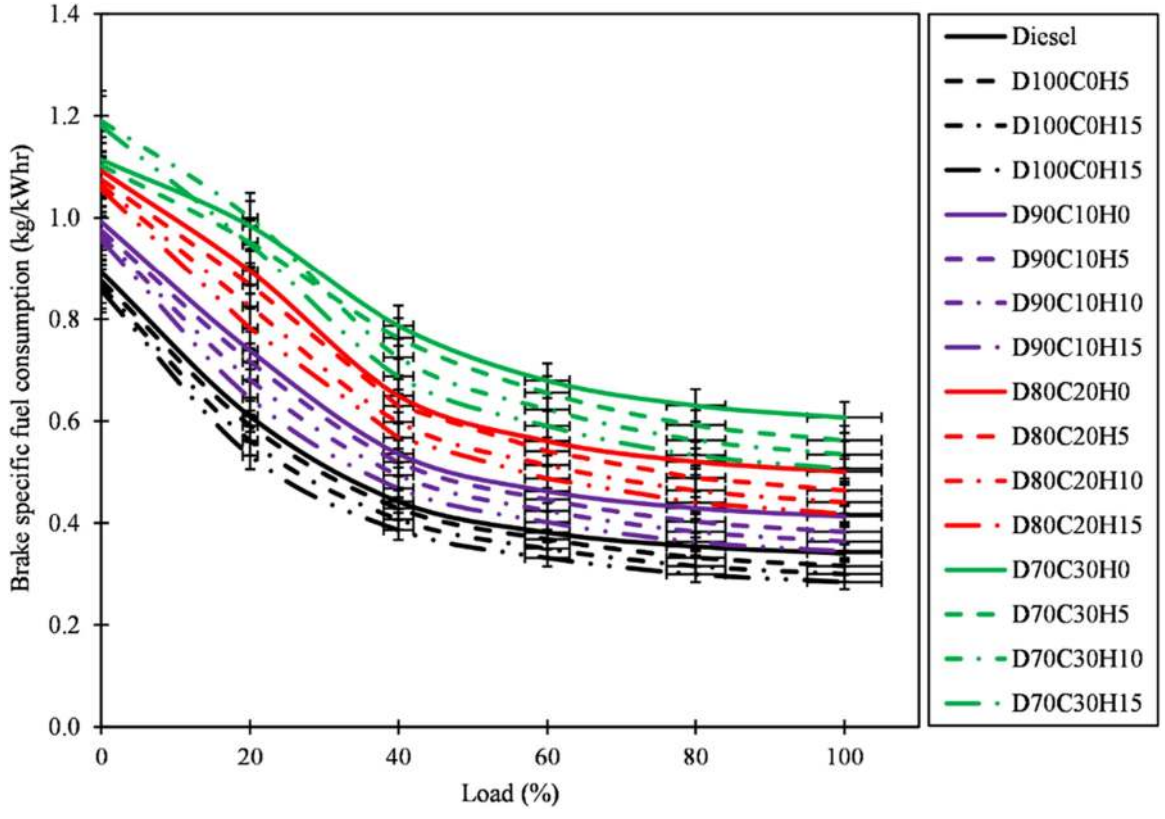


FIGURE 7 | Brake-specific fuel consumption versus load (0%–100% in 20% steps) for diesel and diesel–CIB blends under hydrogen induction 0/5/10/15 L·min^{-1} at constant 1500 rpm speed. CIB, *Calophyllum inophyllum* biodiesel.

BSFC remains higher than neat diesel (e.g., D70C30H15 vs. diesel: +48% at 100% load). At low loads (0%–20%), all fuels exhibit high BSFC. H_2 provides smaller absolute relief (e.g., diesel 0%: 0.892–0.856, 4.0% improvement). Ordering at full load (best to worst BSFC), D100C0H15 (0.284) < D100C0H10 (0.300) < D100C0H5 (0.316) < diesel (0.341) < D90C10H15 (0.345) < D80C20H15 (0.418) < D70C30H15 (0.506).

These benefits are reduced BSFC at higher load when the temperature of the mixture and the turbulence are higher [32]. At low load, the effects of wall heat losses and cycle-to-cycle variability dominate, and therefore, the relative effects of H_2 on BSFC are not as significant. Tightening of the fuel work ratio is caused by thermodynamic advantage and less afterburn as the load increases. The BSFC reduction with H_2 for neat diesel at medium to high loads aligns with recent dual fuel reports that small, metered H_2 fractions advance heat release and reduce incomplete combustion losses, thereby lowering BSFC [14, 15].

BSFC decreased consistently with increasing HEF at each load, at full load with diesel pilot, raising HEF from 3.74% to 11.45%, and reduced BSFC from 0.316 to 0.284 kg·kWh^{-1}. The biodiesel blends exhibited larger BSFC reductions at comparable operating points when described by energy share. For D90C10H5, HEF increased from 3.13% to 9.72% and BSFC reduced from 0.383 to 0.345 kg·kWh^{-1}. For D80C20H5, HEF increased from 2.62% to 8.23% and BSFC reduced from 0.464 to 0.418 kg·kWh^{-1}. For D70C30H5, HEF increased from 2.19% to 6.94% and BSFC reduced from 0.562 to 0.506 kg·kWh^{-1}. These results indicate that the apparent dependence of the H_2 flow largely reflects an HEF shift with load. Table S2 shows the exact HEF corresponding to each reported BSFC trend. Increased HEF tends to reduce BSFC through a combination of direct energy substitution (lower liquid fuel required per unit work) and improved combustion efficiency via faster burning and enhanced oxidation. However, the magnitude of the BSFC improvement remains conditional on mixture preparation and air utilization, which can vary with load and blend properties. Recent dual-fuel investigations reported that fuel consumption benefits track H_2 fraction/energy share [24].

3.5 | Exhaust Gas Temperature

Figure 8 provides a summary of the EGT of all test fuels. EGT increases linearly in all cases. In the case of diesel, EGT increased between 108°C at 0% load to 485°C at 100% load. Increased H_2 in neat diesel increased EGT at all loads, but the difference is not huge at the maximum load (485°C diesel vs. 492°C; 100% load). Greater EGT rises with high H_2 settings (10–15 L·min^{-1}), especially at mid-to-high loads. At 60% load, EGT had risen from 252°C (diesel) to 312°C at 15 L·min^{-1}, and at 80% load, 344°C to 397°C (15.4%). The effect of a higher CIB fraction at a fixed load is lower than that of diesel. EGT dropped to 470°C (100% load, 10% CIB, and 3.1% vs. diesel), 456°C (20% CIB and 6.0%), and 443°C (30% CIB and 8.7%). This decrease is partly neutralized by H_2 induction with regard to the level of blending and flow rate. At 10% CIB and 100% load, the EGT increased to 486°C at 15 L·min^{-1}. In the case of 20% CIB, EGT at 10–15 L·min^{-1} is between 444°C and 462°C (4.7%–8.5% vs. diesel). In the case of 30% CIB, the lowest EGT point was 10 L·min^{-1} (418°C and 13.8% vs. diesel), and it was followed by a very slight increase to 15 L·min^{-1} (439°C and 9.5% vs. diesel).

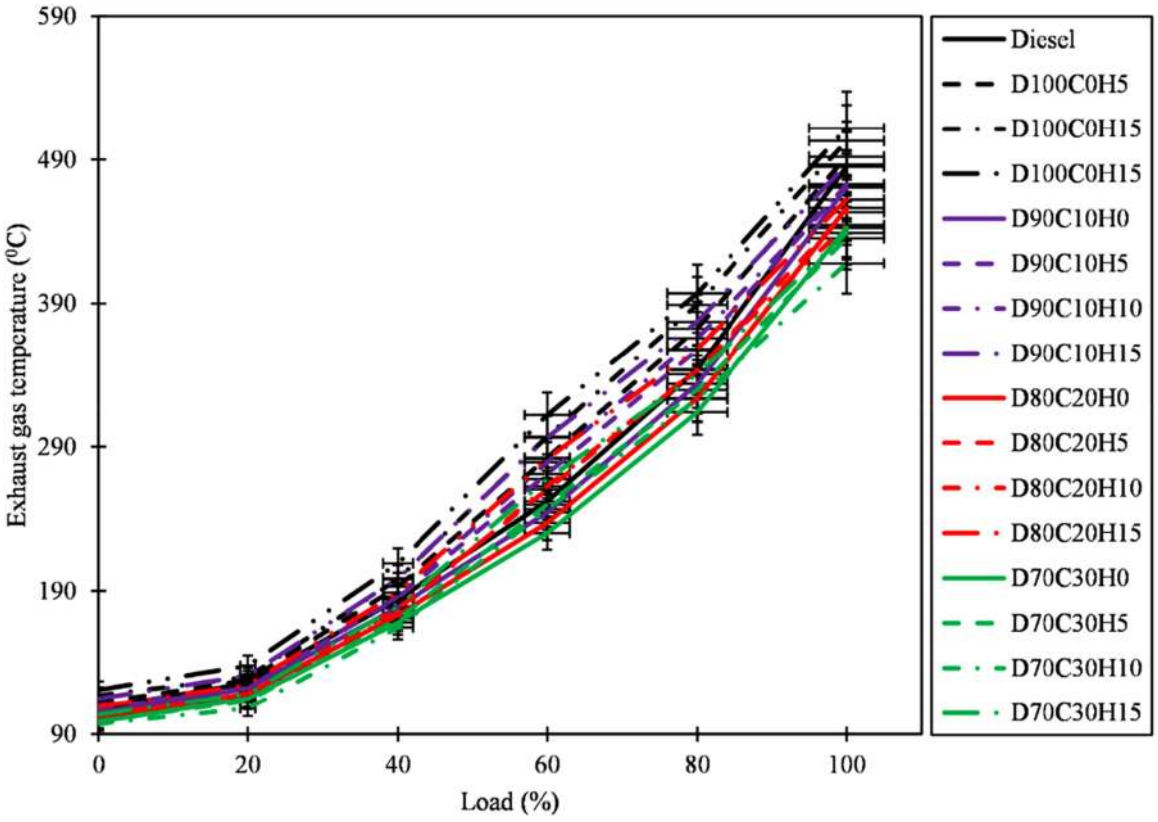


FIGURE 8 | Exhaust gas temperature versus load (0%–100% in 20% steps) for diesel and diesel–CIB blends under hydrogen induction 0/5/10/15 L·min^{-1} at constant 1500 rpm speed. CIB, *Calophyllum inophyllum* biodiesel.

The stronger EGT increase at 10–15 L·min^{-1} of H_2 is observed with neat diesel, which is also compatible with the stronger preference of earlier release of heat and higher bulk gas temperatures as the hydrogen contribution becomes significant. The gradual reduction of EGT with increasing CIB blends implies a net cooling tendency in such conditions, which is consistent with the distribution of energy release and lower exhaust heat at a constant load. H_2 neutralizes a portion of this biodiesel loss of EGT by enhancing the early burning, when operated in tri-fuel mode. Nevertheless, when the CIB share is high (30 vol%), the constraint on mixture preparation may restrain the degree to which hydrogen will be transferred into elevated exhaust temperatures, which is in line with the observed minimum at 10 L·min^{-1} and marginal recovery at 15 L·min^{-1}.

Earlier studies on biodiesel combustion have found lower EGT at similar loads due to variations in heating value and phasing of the combustion process, which decreases exhaust enthalpy [8]. Hydrogen enrichment potentially increases the EGT by increasing early heat release and increasing levels of bulk temperature [12]. Higher biodiesel fractions allow mixture formation and evaporation associated with constraints to moderate the thermal response to hydrogen addition, which is consistent with the reduced EGT recovery in the 30 vol% CIB tri-fuel cases [33].

3.6 | Oxides of Nitrogen

Figure 9 illustrated NO_x variation for all test fuels, which demonstrates strong dependence on load. NO_x increased from 175 ppm at 0% load to 699 ppm at 100% load, for diesel. At a fixed load, increasing hydrogen flow produced a consistent NO_x rise. At 100% load, NO_x increased from 699 ppm (diesel) to 755 ppm at 5 L·min^{-1} (+8.0%), 804 ppm at 10 L·min^{-1} (+15.0%), and 839 ppm at 15 L·min^{-1} (+20.0%). The same ordering is observed at 60% load, where NO_x increased from 406 ppm (diesel) to 439 ppm (+8.1%), 467 ppm (+15.0%), and 487 ppm (+20.0%) with 5/10/15 L·min^{-1}. Biodiesel addition without hydrogen caused only small upward shifts at matched load: at 100% load, D90C10H0 is +2% relative to diesel, while D80C20H0 and D70C30H0 are +4%–5%. Considering the combined uncertainty, the +2% change is treated as marginal, whereas the +4%–5% increases indicate a weak but repeatable upward tendency. Under tri-fuel operation at 100% load with 15 L·min^{-1} hydrogen, NO_x increased to 856 ppm (+22.5%) for D90C10H15, 872 ppm (+24.8%) for D80C20H15, and 881 ppm (+26.1%) for D70C30H15 relative to diesel.

The high-load dependence is associated with the higher in-cylinder temperature and the availability of high-temperature time when the load increases. This enhancement of NO_x with hydrogen flow at both loadings is consistent with an elevated temperature, more reactive combustion process that raises the peak temperatures and maintains high-temperature regions longer. The smallest increment is within experimental uncertainty, and the remaining +4%–5% shifts are interpreted conservatively as a modest temperature/oxygen availability effect that becomes more visible at higher blend levels. In tri-fuel cases, the elevated NO_x levels at high load reflect the combined influence of hydrogen reactivity together with oxygenated liquid fuel effects on mixture oxidation.

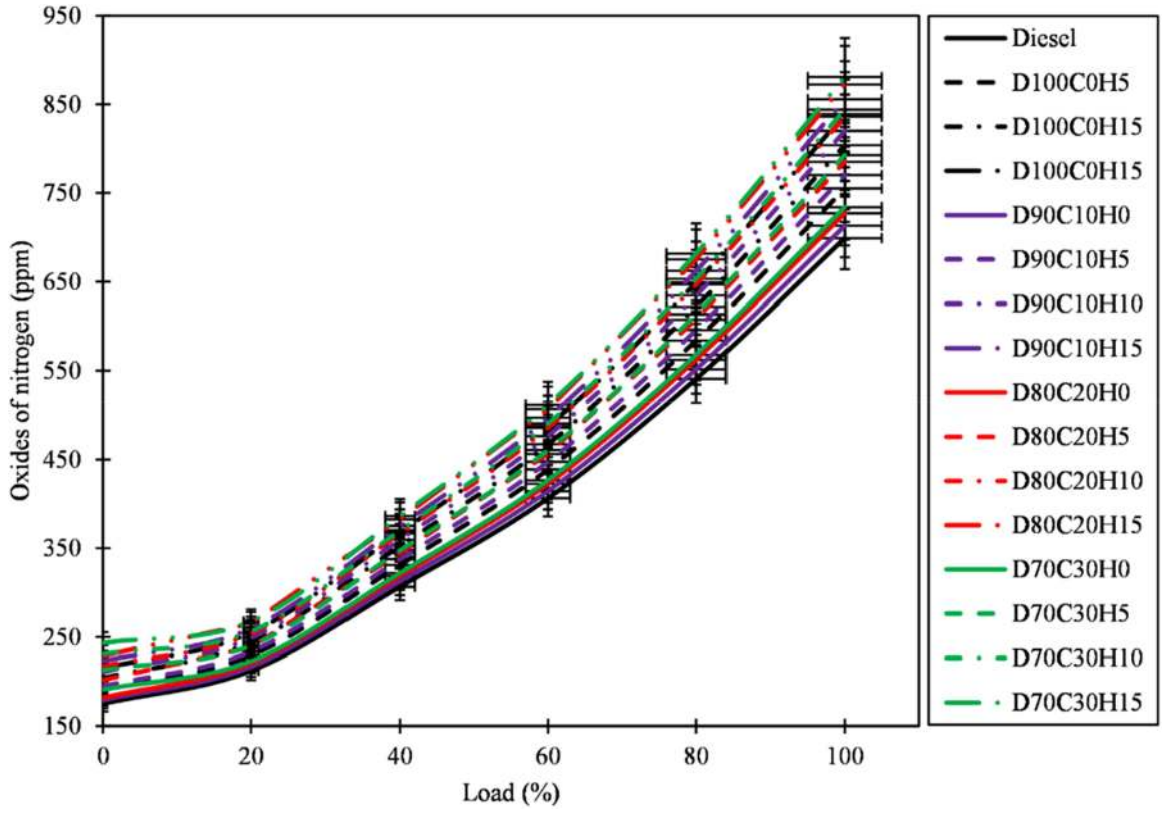


FIGURE 9 | Oxides of nitrogen versus load (0%–100% in 20% steps) for diesel and diesel–CIB blends under hydrogen induction 0/5/10/15 L·min^{-1} at constant 1500 rpm speed. CIB, *Calophyllum inophyllum* biodiesel.

These trends are consistent with temperature-controlled NO formation, described by the extended Zeldovich mechanism, where higher peak temperature and longer residence time accelerate NO_x production [34]. Prior hydrogen-enriched diesel and hydrogen–biodiesel studies similarly reported NO_x increase with increasing hydrogen share, particularly at mid-to-high loads, and attributed the effect to advanced/accelerated heat release and elevated thermal conditions [27, 35].

3.7 | Hydrocarbon

Figure 10 shows HC variations for all test fuels. HC decreases monotonically with load for every case. For diesel, HC declines from 71.35 ppm at 0% load to 18.48 ppm at 100% load (74% reduction). At a fixed load, increasing hydrogen flow reduces HC consistently. At 100% load for diesel, HC decreases from 18.48 to 12.94 ppm at 10 $L{\cdot}min^{-1}$ (30.0% reduction) and to 10.16 ppm at 15 $L{\cdot}min^{-1}$ (45.0% reduction). A similar pattern is observed at midload: at 40% load, HC decreases from 33.28 ppm (diesel) to 24.70 ppm at 10 $L{\cdot}min^{-1}$ (25.7% reduction) and to 19.40 ppm at 15 $L{\cdot}min^{-1}$ (41.7% reduction). CIB blends with matched load in the absence of hydrogen also decrease HC compared with diesel. The highest HC reduction occurs under tri-fuel operation at high load. As compared with diesel at 100% load, HC is reduced by 53%, 56%, and 59% in the case of D90C15H15, D80C20H15, and D70C30H15, respectively.

The HC decrease with increasing hydrogen flow at fixed load indicates more complete oxidation, consistent with a stronger early heat release and enhanced combustion stability when hydrogen contribution increases. The additional HC reduction observed with CIB blending is consistent with improved oxidation in locally rich zones due to fuel-bound oxygen, which can reduce the persistence of partially oxidized hydrocarbons. In tri-fuel cases, the combined effects of hydrogen-assisted reactivity and oxygenated liquid fuel appear additive at high load, yielding the observed 50%–60% HC reductions relative to diesel. At very low loads (0%–20%), residual HC remains comparatively high across fuels, suggesting that low bulk gas temperature and incomplete oxidation constrain HC burnout even when hydrogen is present.

Hydrogen-assisted and oxygenated fuel combustion studies reported reductions in HC with increasing load and with increased hydrogen share, attributed to improved oxidation kinetics and reduced misfire/partial-burn tendencies at higher thermal states [13, 36]. Similarly, oxygenated biodiesel blends are often associated with lower HC at matched operating points due to enhanced oxidation of fuel-rich regions, while low-load conditions remain challenging for complete HC burnout because of lower temperature and shorter oxidation time [15].

3.8 | Carbon Monoxide

Figure 11 presents CO variations for all test fuels. CO generally decreases with load from 0% to 80% for all cases, while diesel exhibits a marked increase at 100% load. For diesel, CO reduces from 0.30 vol% at 0% load to 0.21 vol% at 80% load, then increases to 0.45 vol% at 100% load. At matched load, stepwise increases in hydrogen flow reduce CO relative to the corresponding no-hydrogen case. The strongest CO suppression is recorded under tri-fuel operation. At 100% load, CO drops to

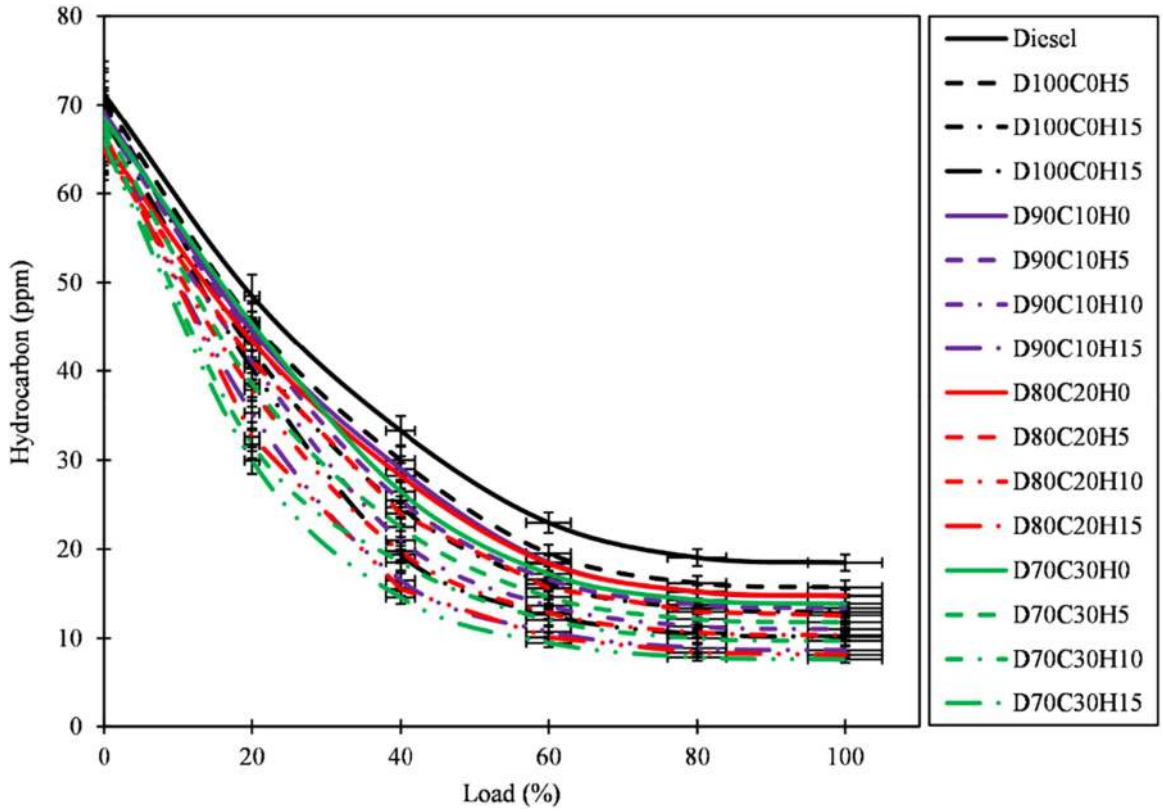


FIGURE 10 | Hydrocarbon emissions versus load (0%–100% in 20% steps) for diesel and diesel–CIB blends under hydrogen induction 0/5/10/15 $L{\cdot}min^{-1}$ at constant 1500 rpm speed. CIB, *Calophyllum inophyllum* biodiesel.

0.171 vol% for D90C10H15 (62.0% reduction vs. diesel), 0.151 vol % for D80C20H15 (66.4% reduction), and 0.141 vol% for D70C30H15 (68.7% reduction).

The diesel CO rise at full load is consistent with richer local combustion and oxidation under high fueling, which increases the persistence of partially oxidized carbon species. The CO reduction with increasing hydrogen flow indicates more complete oxidation at a given load, consistent with improved combustion completeness when hydrogen contribution increases. The enhanced reductions under tri-fuel operation suggest a combined effect: hydrogen strengthens overall oxidation propensity, while the oxygenated liquid fuel supports oxidation in locally rich zones that would otherwise contribute disproportionately to CO at high load. At low loads, the benefit of small hydrogen addition can be weaker because lower in-cylinder temperature and pressure constrain oxidation kinetics; in contrast, higher hydrogen induction improves mixture reactivity and charge conditioning sufficiently to suppress CO formation more consistently.

Hydrogen-enriched diesel combustion studies reported CO reductions with increasing hydrogen share, attributed to improved mixture preparation and accelerated oxidation, particularly under higher load thermal conditions [24, 25]. Likewise, oxygenated biodiesel blends are frequently associated with reduced CO at comparable loads due to improved oxidation in fuel-rich regions, which becomes especially relevant near full-load diffusion-controlled combustion regions [24, 25].

3.9 | Carbon Dioxide

Figure 12 shows CO_2 variations for all test fuels. CO_2 increases linearly with load for every case. For diesel, CO_2 increased from 2.14 vol% at 0% load to 9.88 vol% at 100% load (+7.74 vol%). At matched load, hydrogen induction produced only a small decrease in measured CO_2 concentration. For neat diesel at 100% load, CO_2 decreased from 9.88 to 9.78 vol% (5 $L{\cdot}min^{-1}$ and −1.0%), 9.68 vol% (10 $L{\cdot}min^{-1}$ and −2.0%), and 9.58 vol% (15 $L{\cdot}min^{-1}$ and −3.0%). Tri-fuel cases showed a similar small reduction at high load; for example, D70C30H15 recorded 9.58 vol% at 100% load (−3.0% vs. diesel), with comparable 3% decreases also observed at 80% and 60% load. The observed CO_2 changes associated with hydrogen addition are $\leq 3\%$ across 5–15 $L{\cdot}min^{-1}$ and are near the combined uncertainty and sampling scatter for steady-state concentration measurements.

CO_2 rise primarily reflects higher carbon conversion rates and increased total fuel input as brake load increases under constant-speed operation. The small CO_2 reductions observed with hydrogen addition are consistent with partial carbon energy displacement by a carbon-free fuel, which can lower exhaust CO_2 concentration at comparable load even when combustion completeness improves. Because the magnitude of the CO_2 differences ($\leq 3\%$) lies close to the comparative uncertainty band for concentration measurements, CO_2 is interpreted conservatively as a qualitative indicator of combustion/carbon throughput changes rather than as a statistically separable reduction metric across fuels.

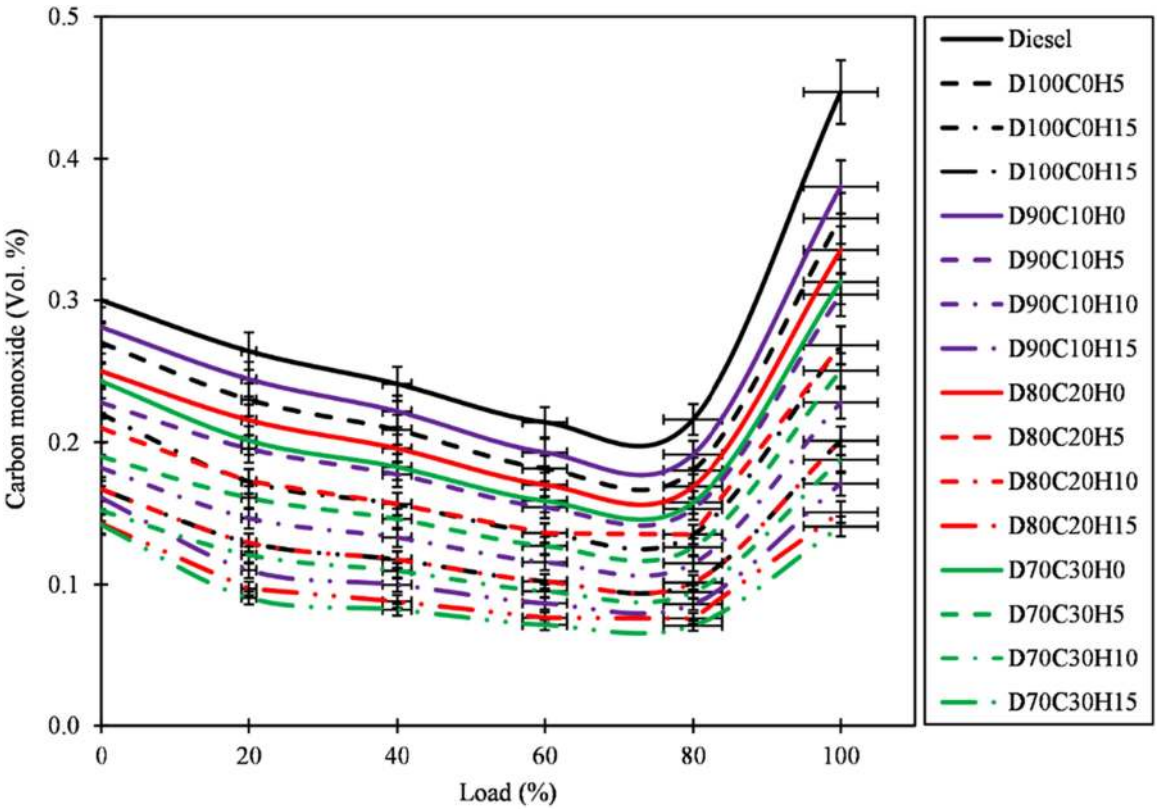


FIGURE 11 | Carbon monoxide emissions versus load (0%–100% in 20% steps) for diesel and diesel–CIB blends under hydrogen induction 0/5/10/15 $L{\cdot}min^{-1}$ at constant 1500 rpm speed. CIB, *Calophyllum inophyllum* biodiesel.

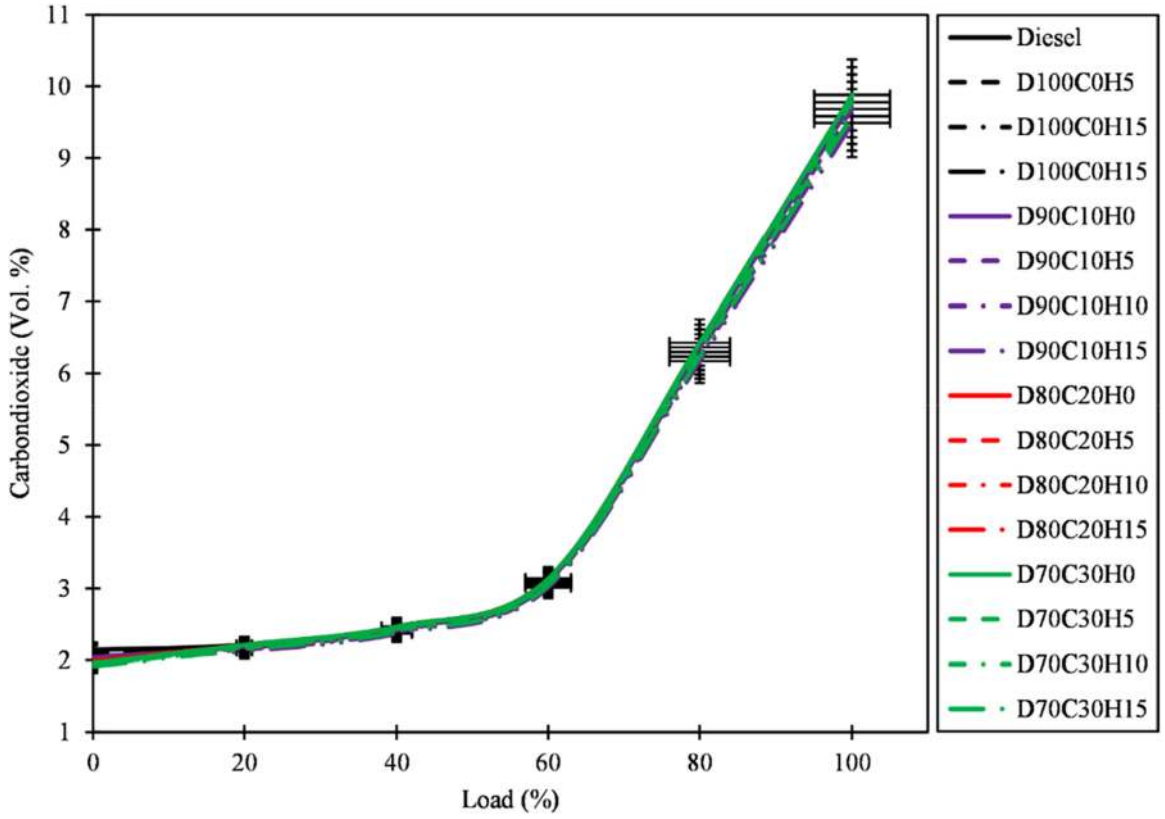


FIGURE 12 | Carbon dioxide emissions versus load (0%–100% in 20% steps) for diesel and diesel–CIB blends under hydrogen induction 0/5/10/15 L·min^{-1} at constant 1500 rpm speed. CIB, *Calophyllum inophyllum* biodiesel.

Previous hydrogen-assisted diesel studies reported similar behavior, where a small amount of hydrogen substitution can slightly reduce exhaust CO_2 concentration at matched load by reducing carbon throughput, while simultaneous reductions in CO and HC indicate improved oxidation completeness [7].

3.10 | Smoke

Figure 13 summarizes smoke opacity for all test fuels. Smoke increases linearly with load for every case. For diesel, smoke increased from 14.56% opacity at 0% load to 45.84% at 100% load. Hydrogen induction produced strong smoke suppression at matched load, with the magnitude increasing with hydrogen flow. At 100% load for neat diesel, smoke decreased from 45.84% to 32.09% at 5 L·min^{-1} (30% reduction), to 22.92% at 10 L·min^{-1} (50% reduction), and to 16.04% at 15 L·min^{-1} (65% reduction). A similar pattern was observed at 80% load, where smoke decreased from 36.84% (diesel) to 25.79% (5 L·min^{-1} and 30% reduction), 18.42% (10 L·min^{-1} and 50% reduction), and 12.98% (15 L·min^{-1} and 65% reduction). Under tri-fuel operation, the largest reductions occurred at high load. At 100% load, smoke decreased to 12.84% for D90C10H15 (72% reduction vs. diesel), 11.23% for D80C20H15 (75% reduction), and 10.43% for D70C30H15 (77% reduction).

Smoke reduction with increasing hydrogen flow is consistent with a progressive shift away from soot-forming diffusion-controlled burning toward cleaner combustion at the same load. The further reduction observed under tri-fuel operation indicates an additional oxidation advantage when CIB is present alongside hydrogen, consistent with improved burnout of soot precursors and reduced persistence of locally rich zones under high-load conditions. Hydrogen-enriched diesel combustion studies reported suppression in smoke because hydrogen contains no carbon and can reduce soot-forming rich zones while strengthening oxidation pathways, leading to large opacity reductions at mid-to-high loads [22, 37]. Oxygenated biodiesel blends similarly promote oxidation of soot precursors and reduce smoke relative to diesel; when combined with hydrogen, these effects can be additive, producing stronger smoke suppression than either approach alone [8, 22].

3.11 | Inlet HEF Across Blends and Loads

The variations in inlet HEF across diesel, D90C10, D80C20, and D70C30 with respect to load for H_2 volume fraction of 5, 10, and 15 L·min^{-1} are presented in Figure 14a–d, respectively, and the data set is presented in Table S2. The inlet HEF varied 2.19%–25.7% across the test matrix, rising with H_2 setpoint and falling with load. At 20% load, inlet HEF averaged 7.6%, 14.4%, and 21.0% for 5, 10, and 15 L·min^{-1}, respectively. At 80% load, the corresponding means declined to 3.45%, 6.98%, and 10.60%. The minimum inlet HEF occurred at D70C30H5 at 100% load (2.19%), while the maximum occurred at D100C0H15 at 20% load (25.69%). At a fixed H_2 flow, higher diesel shares yielded a larger inlet HEF (e.g., at 10 L·min^{-1}, the mean inlet HEF increased from 7.06% for D70C30 to 11.58% for D100C0), consistent with lower liquid fuel demand (lower BSFC and higher blend LHV).

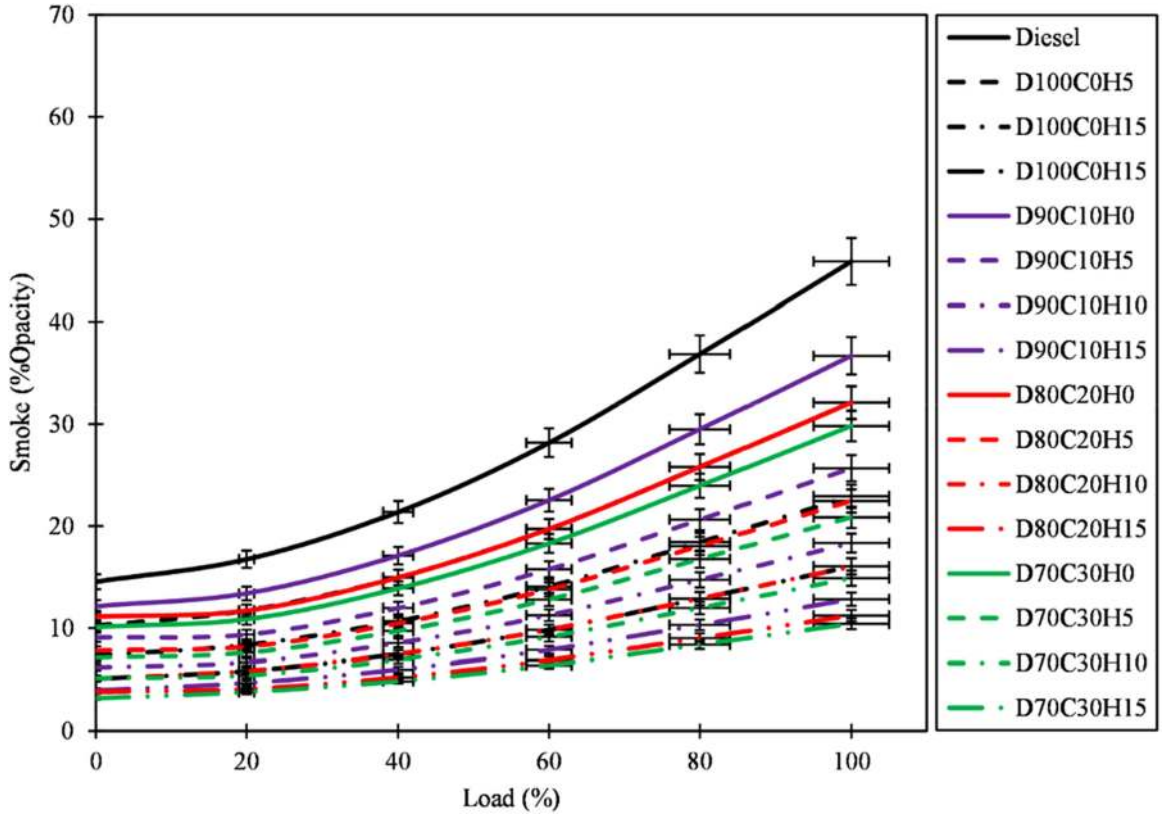


FIGURE 13 | Smoke opacity versus load (0%–100% in 20% steps) for diesel and diesel–CIB blends under hydrogen induction 0/5/10/15 L·min^{-1} at constant 1500 rpm speed. CIB, *Calophyllum inophyllum* biodiesel.

$\dot{Q}_{H_2}$ is fixed by standard liters per minute (SLPM) at the MFC reference conditions, whereas $\dot{Q}_{liq}$ increases with brake power and typically with load. Consequently, inlet HEF declines at higher loads unless H_2 flow is scaled. This load dependence is an established feature of diesel–H_2 dual-fuel operation and appears through recent studies using manifold-inducted H_2. Guan et al. [38] (heavy duty and premanifold H_2) reported that the effective H_2 share must increase with load to maintain similar combustion impacts; otherwise, inlet HEF falls and the dual-fuel effect weakens. Ekin et al. [39] similarly show stronger H_2 influence at partial loads than at full load when SLPM is held constant. The observed blend ordering of inlet HEF (D100C0 > D90C10 > D80C20 > D70C30) reflects changes in blend LHV and BSFC. Recent biodiesel–H_2 studies note similar behavior as the oxygenated liquid increases liquid energy demand per unit brake work, lowering the relative gas share at a fixed SLPM [31].

3.12 | Bootstrapped Empirical Multiobjective Ranking and Selection

BEMORS converts the eight metric outcome vector y, which prioritizes complete oxidation (low CO/HC) while tracking CO_2 as an indicator of completeness, into robust, unit interval scores via percentile scaling and direction unification, then draws random utility vectors w from a Dirichlet prior to estimate selection probability π_i of each experiment. The baseline prior is Dirichlet ($\alpha = 1$) (uniform over the simplex), with $R = N_{MC}$ Monte Carlo draws. Uncertainty is reported as Wilson 95% CIs and bootstrap bands from $B = [N_{boot}]$ resamples of the scaling step. The Pareto set, dominance gaps, and HV provide geometric diagnostics. The eight-objective BEMORS ranking is not interpreted as an abstract score aggregation. Rather, each high probability operating point is read as a specific combustion region observed in Section 3.1. In the considered data set, higher BTE/lower BSFC configurations coincide with more intense early heat release (higher premixed contribution), which tends to elevate burned gas temperature and therefore NO_x. Whereas lower smoke points align with reduced diffusion flame dominance due to carbon displacement by H_2 and oxidation from biodiesel. Consequently, the selection probabilities reported are interpreted as probabilistic preferences over physically distinct trade-off regions.

3.12.1 | *Sanity Checks and Pareto Set*

All eight metrics occupy the (0, 1) score range without boundary pileups (Figure 15). No single axis dominates after direction unification, indicating that the quantile scalers remove tail leverage while preserving ranking information. The nondominated set Ω contains (K) experiments ((K/N) of all runs). As anticipated from single metric panels, the front is populated by hydrogenated cases at medium/high load and CIB with H_2 at higher biodiesel shares, whereas neat biodiesel is largely dominated due to BSFC/NO_x trade-offs (Figure 16). Similar observations were reported by Pelissari et al. [40]. Dominance-gap plots (Figure 17) confirm that low-load points are far from Ω (large L_1 gaps), consistent with their poorer BTE and higher BSFC/HC/CO.

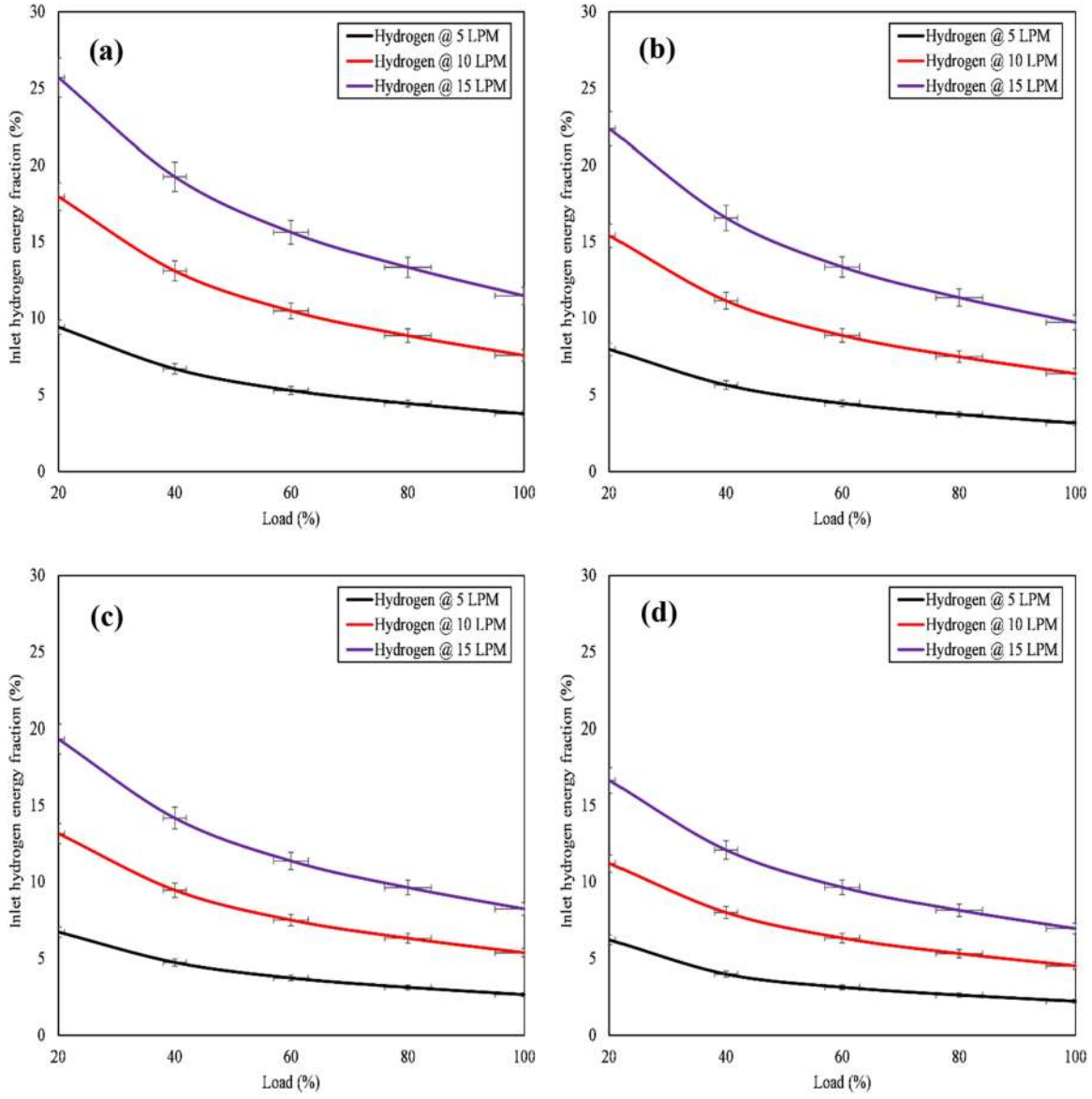


FIGURE 14 | Inlet hydrogen energy fraction (HEF, %; LHV basis) versus load for (a) D100C0, (b) D90C10, (c) D80C20, and (d) D70C30 under hydrogen induction 5/10/15 $L \cdot min^{-1}$ at constant 1500 rpm speed. HEF, hydrogen energy fraction; LHV, lower heating value; LPM, liters per minute.

3.12.2 | *Preference-Agnostic Winners (baseline $\alpha = 1$)*

The best Dirichlet experiments are given in Table 5. Exp. No. 21, that is, D100C0H15 at 40% load, becomes top-1 with BEMOR probability of 0.13525. This trend demonstrates constant superiority. Analysis of standardized results indicates that Exp. No. 21 performs best with high BTE/CO_2 and low Smoke/CO/HC without extreme NO_x and that is exactly the balance of multi-pollutants desired in this instance (Figure 18). Rank 1 (D100C0H15 at 40% load) is an intermediate load area where the inducted H_2 fraction is still high enough to enhance early combustion. Furthermore, it inhibits soot precursors and peak temperature exposure is moderate in comparison to high-load operation [41]. This is in accordance with the experimentally observed trend that the midloads points can provide a decrease in the incomplete combustion indicators (CO/HC) and smoke, without the high NO_x gain. Nevertheless, this would have been experienced by the identical quantity of H_2 flow at greater loads. The two near-tie candidates are physically consistent alternatives, that is, high-load points can be competitive in efficiency/smoke but become weak in NO_x scenarios, and biodiesel blends at midload points become competitive when soot is co-opted.

The most balanced range of loading (40%–60%) and 15 $L \cdot min^{-1}$ H_2 creates midload cases with good smoke suppression, moderate NO_x, and acceptable efficiency. The high-load cases (80%–100% load) are further divided into efficiency-leading and cleaner combustion cases with reduced CO/HC and smoke, but still with consistently high NO_x because of increased thermal severity. Tri-fuel points have a tendency to enhance smoke/CO/HC, especially at midload, at high biodiesel shares the efficiency cost is more evident and the full-load NO_x is the limiting factor. The low-load points (20% load) can be seen as boundary points where smoke-free operation is possible, but performance is poor and remnant HC remains, which points to the operational drawback of low-temperature oxidation at light-load conditions.

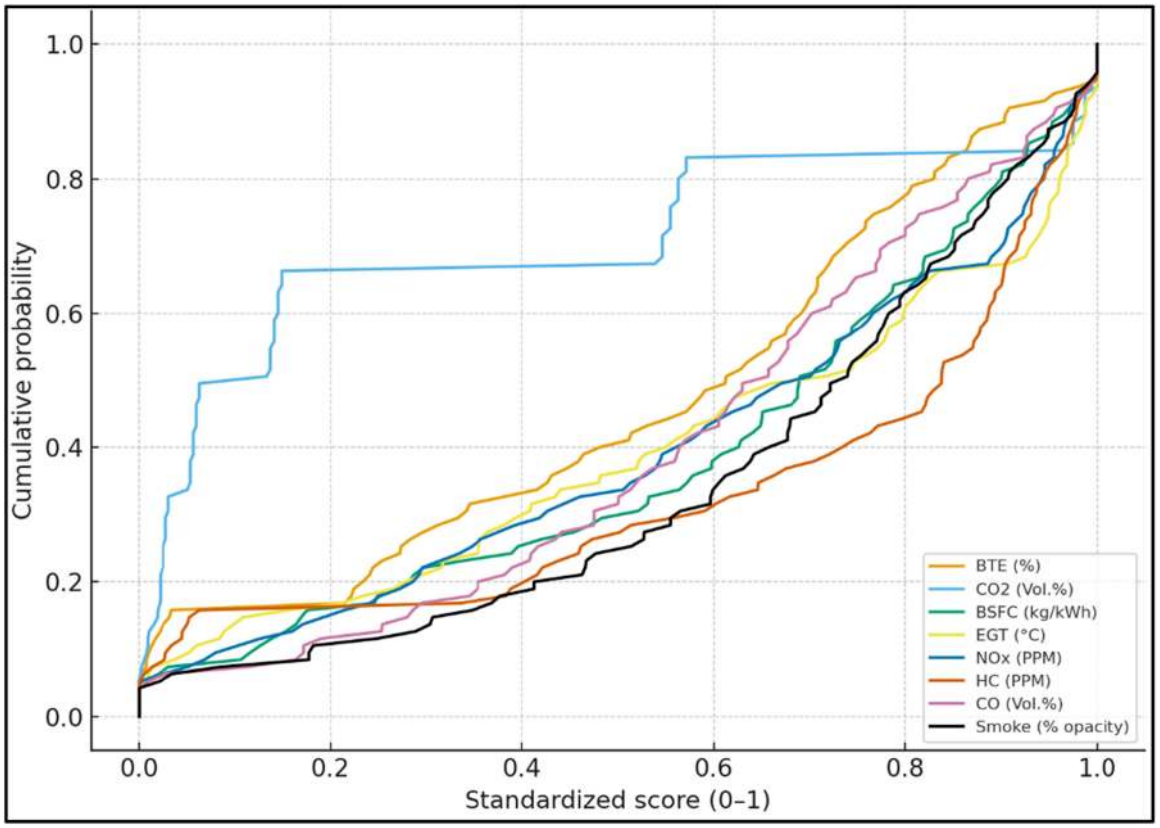


FIGURE 15 | Empirical CDFs of the eight normalized performance-emissions criteria over the 96-point tri-fuel data set after quantile scaling and direction unification. BSFC, brake specific fuel consumption; BTE, brake thermal efficiency; CDFs, cumulative distribution functions; EGT, exhaust gas temperature.

3.12.3 | *Weight Prior Sensitivity (Dirichlet α Sweep)*

Figure 19 presents the stability of preference-agnostic selection across sweeps $\alpha \in \{0.25, 0.5, 1, 2, 4\}$. For $\alpha < 1$ (sharp and single-issue preferences), selection mass shifts modestly toward experiments excelling on one axis (e.g., lowest Smoke or lowest BSFC), but Exp. No. 1 remains top ranked. For $\alpha > 1$, probabilities flatten, yet the top-3 identity is unchanged. The best experimental run is prior robust and plausible stakeholder heterogeneity does not overturn rankings [18].

3.12.4 | *Policy Scenarios*

To reflect regulatory preferences, the Dirichlet weight prior was skewed toward emissions. Scenario A (NO_x upweighted) used $\alpha_{NO_x} = 2$ and $\alpha_{j \neq NO_x} = 1$. Scenario B (NO_x + Smoke upweighted) used $\alpha_{NO_x} = \alpha_{Smoke} = 2$ with all others = 1. Selection probabilities π_i were computed from $R = 20{,}000$ utility draws on the standardized eight-metric score space (maximize, BTE and CO_2; minimize, BSFC, EGT, NO_x, HC, CO, and Smoke).

At baseline ($\alpha = 1$), the top-3 were as follows:

- D100C0H15_L40: $\pi = 0.1352$.
- D90C10H15_L80: $\pi = 0.0965$.
- D100C0H15_L80: $\pi = 0.0937$.

Under NO_x upweighted,

- D100C0H15_L40 increases to $\pi = 0.1833$ ($\Delta\pi = +0.0480$), remaining rank-1.
- D100C0H15_L60 rises into rank-2: $\pi = 0.0939$ ($\approx$ baseline 0.0931).
- D100C0H15_L20 emerges as rank-3: $\pi = 0.0909$.
- Notably, D90C10H15_L80 falls to $\pi = 0.0540$ ($\Delta\pi = -0.0425$), and D100C0H15_L80 to $\pi = 0.0656$ ($\Delta\pi = -0.0281$).

Under NO_x + Smoke upweighted,

- D100C0H15_L40 stays first at $\pi = 0.1669$ ($\Delta\pi = +0.0316$ vs. baseline).
- D80C20H15_L40 moves up strongly to $\pi = 0.0932$ ($\Delta\pi = +0.0296$), taking rank-2.
- D90C10H15_L20 enters as rank-3 at $\pi = 0.0890$.
- High-load H_2 cases with excellent efficiency (D90C10H15_L80 and D100C0H15_L80) decline further (to $\pi = 0.0436$ and 0.0350, respectively), consistent with the smoke/NO_x emphasis.

NO_x upweighting favors moderate to high reactivity at midloads, where peak temperature exposure and residence time can be moderated without abandoning the H_2-enabled gains in BTE/smoke. This explains that D100C0H15 at 40%–60% load consolidates rank (π: 0.1352–0.1833 at L40 and 0.0931–0.0939 at L60), while very high-load settings are not advisable for NO_x share. With the further upweighting of the Smoke parameter, there is also a shift in the selector to oxygenated blends at midload. D80C20H15_L40 increases considerably, rising from 0.0636 to 0.0932, as a result of the combination of high premixed reactivity

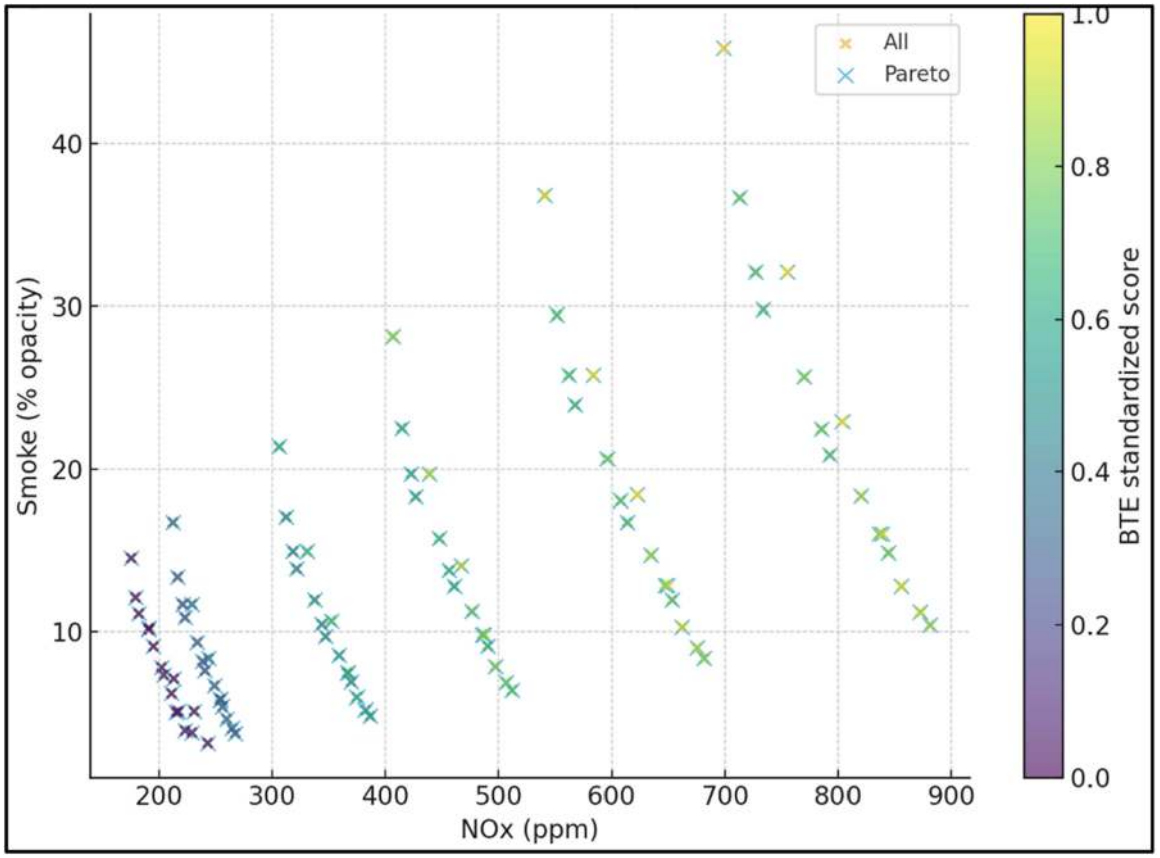


FIGURE 16 | Two-dimensional trade-off plane between NO_x and smoke (standardized scores) for all 96 operating points, where the points indicate the feasible set used for Pareto screening and robustness analysis. BTE, brake thermal efficiency.

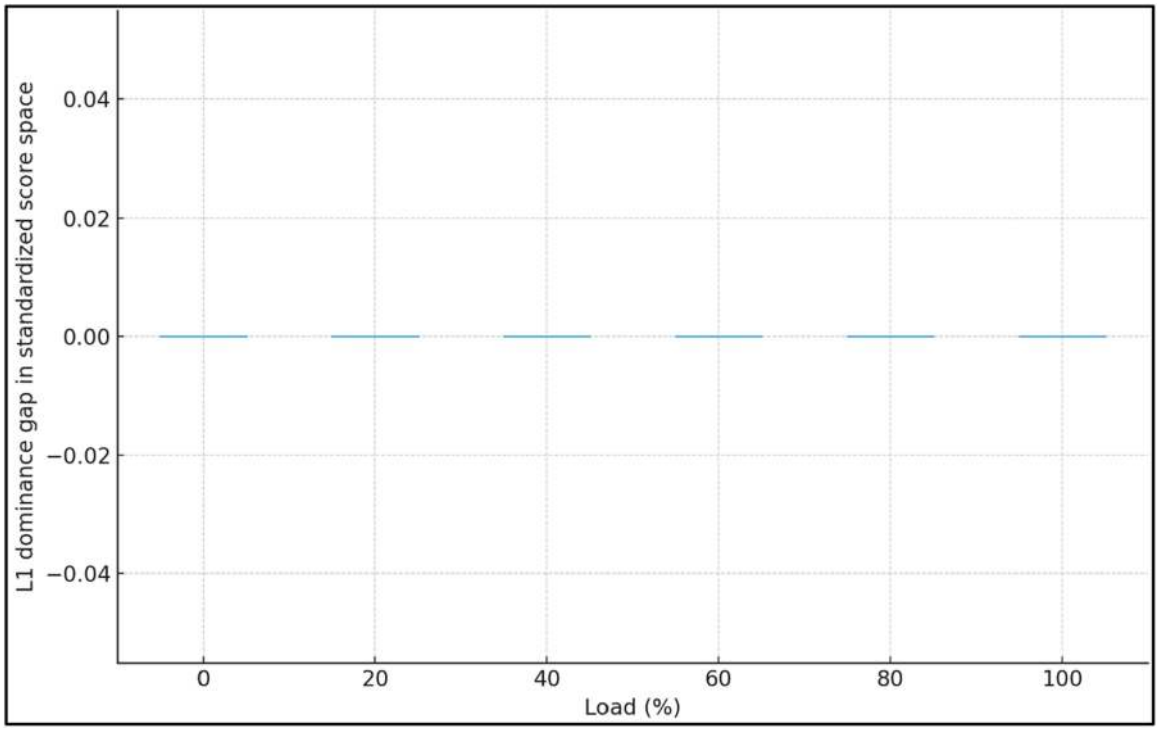


FIGURE 17 | Optimal dominance-gap diagnostic across the 96-point data set, showing the separation between the best compromise candidates and their nearest dominating/competing neighbors (lower gap indicates tighter competition near the front).

TABLE 5 | The list of top-10 experiments by uniform Dirichlet.

Exp. no.	Diesel (vol%)	CIB (vol%)	Hydrogen ($L \cdot min^{-1}$)	Load (%)	Pareto	BEMORS probability	BEMORS rank	Physical signature
21	100	0	15	40	True	0.13525	1	Midload balanced corridor, low smoke with moderate NO_x, and acceptable efficiency
47	90	10	15	80	True	0.0965	2	High-load clean combustion point, very low CO/HC, and reduced smoke, but NO_x is elevated
23	100	0	15	80	True	0.0937	3	High-load efficiency leader, highest BTE/lowest BSFC among top candidates; smoke and NO_x remain high
22	100	0	15	60	True	0.0931	4	Mid–high-load compromise, strong efficiency with controlled smoke and moderate NO_x
69	80	20	15	40	True	0.06365	5	Midload ultra-low smoke corridor, best smoke suppression with moderate NO_x, but weaker efficiency
93	70	30	15	40	True	0.05945	6	Midload lowest smoke extreme, minimum smoke, and low CO, but high BSFC/low BTE
96	70	30	15	100	True	0.05735	7	Full-load oxygenated tri-fuel, moderate efficiency, and reduced smoke/HC, but very high NO_x and high thermal severity
72	80	20	15	100	True	0.05655	8	Full-load performance, cleaning compromise, higher efficiency than 30% CIB at full load with low smoke/HC, but NO_x remains very high
92	70	30	15	20	True	0.04925	9	Low-load incomplete combustion corridor, very low smoke but very poor efficiency (high BSFC/low BTE) with residual HC
20	100	0	15	20	True	0.0387	10	Low-load H_2 assist corridor, better efficiency than high- CIB low-load case, but HC remains high, and gains are limited by low-load oxidation constraints

Abbreviations: BEMORS, Bootstrapped Empirical Multiobjective Ranking and Selection; BSFC, brake specific fuel consumption; BTE, brake thermal efficiency; CIB, *Calophyllum inophyllum* biodiesel.

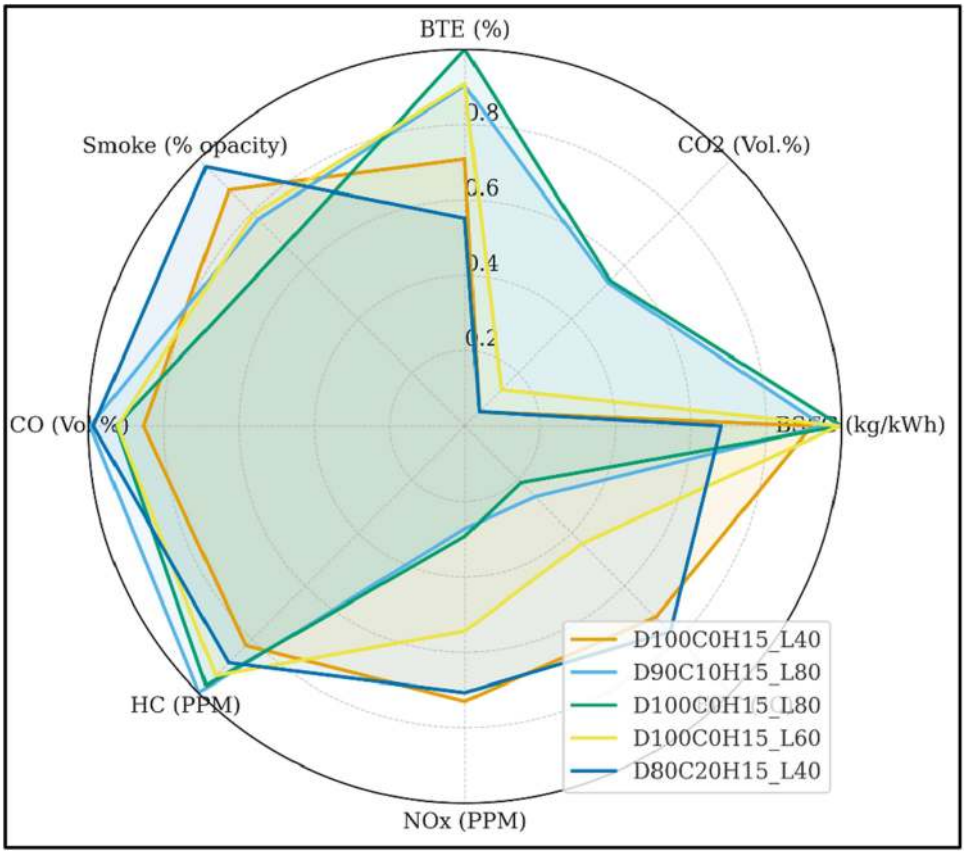


FIGURE 18 | Top-5 experiments by preference-agnostic selection probability (Dirichlet $\alpha = 1$): standardized metric profiles. CIB, *Calophyllum inophyllum* biodiesel.

(H_2) with fuel-bound oxygen (biodiesel), producing a cleaner soot path that demonstrates only a small efficiency cost. The 20% load entries in the solution set, D100C0H15_L20 and D90C10H15_L20, under policy priority, suggest that low-to-mid load regions can produce simultaneous NO_x and smoke reduction, even though they are not globally efficient at $\alpha = 1$.

D100C0H15_L40 is the decision-grade option in the case of fleets that value efficiency and opacity, with D90C10H15_L80 and D100C0H15_L80 being the nearest to it. The H_2 frequency of 15 L·min^{-1} may be accepted in the case of NO_x-centric policy, and 40%–60% load is recommended with maximum probabilities of the best settings existing (e.g., 0.1833 at L40). Small retard/EGR might be modified on the condition of additional reduction of NO_x. With NO_x + Smoke limits, switch to either H_2 at 20% CIB at 40% load (D80C20H15_L40, 0.0932) or neat diesel at 40% load according to limits on the opacities and duty cycle.

These shifts mirror the grouped probability bars in Figure 20 (baseline vs. NO_x upweighted) and Figure 21 (baseline vs. NO_x + Smoke upweighted). The ranking is directionally stable across the Dirichlet concentration sweep [41, 42]. Top identities persist while probabilities flatten or sharpen with α, indicating prior robust conclusions rather than instability to preference uncertainty [43].

3.12.5 | *Bootstrap Stability (Normalization Uncertainty)*

Across bootstraps, π_i bands for the top-5 remain nonoverlapping with the bulk of candidates (Figure 22). To quantify sensitivity to the empirical scalers, the 5%–95% quantiles used for unit interval normalization were re-estimated over $B = 30$ bootstrap resamples (rowwise resampling). For each bootstrap, metrics were rescaled and the preference-agnostic selector was reapplied with Dirichlet($\alpha = 1$), using $R = 1500$ utility draws, bootstrap means, and 95% bands (2.5–97.5th percentiles) were reported for the top-5 baseline experiments.

Stability is strongest for the leading configuration D100C0H15_L40, whose selection probability centers at 0.1384 with a relatively narrow band (0.1063, 0.1633), and the full data baseline 0.1242 lies well inside this interval. D100C0H15_L60 is likewise stable (mean 0.0910, band (0.0571, 0.1218)). Experiments that straddle the front but trade-offs on at least one axis show wider bands, notably D100C0H15_L80 (mean 0.1001, band (0.0094, 0.1814)) and D90C10H15_L80 (mean 0.0819, band (0.0296, 0.1296)). The biodiesel-enriched midload option D80C20H15_L40 remains competitive yet clearly below the best setting (mean 0.0679, band (0.0373, 0.1006)).

The rank-1 identity is robust to plausible variation in the scaling quantiles. Its π-band does not overlap with the majority of nonwinners and only marginally overlaps the tail of a single near tie. Wider bands observed for high-load H_2 cases reflect that small changes in normalization (especially on NO_x/smoke tails) modestly tilt the utility surface, but the central tendency preserves the qualitative ordering seen with full data scaling [44].

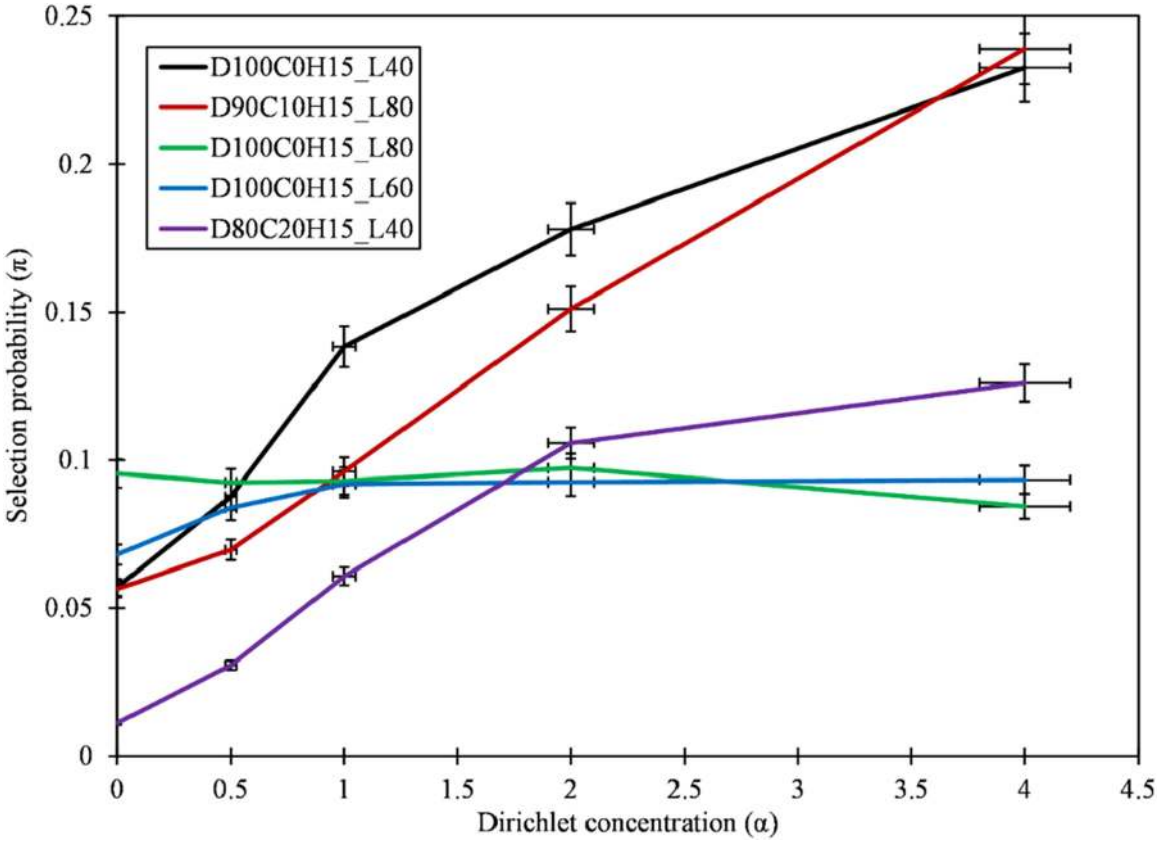


FIGURE 19 | Stability of preference-agnostic selection across α (top-5 tracked).

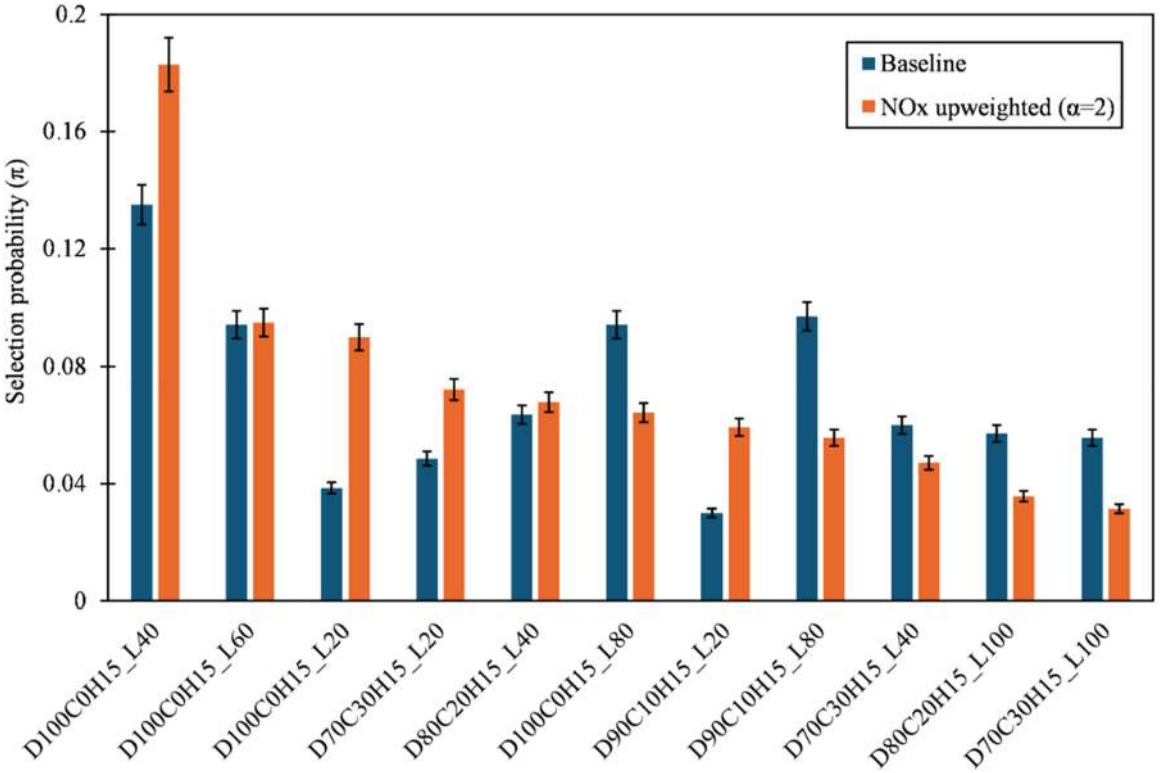


FIGURE 20 | Selection probabilities: baseline versus NO_x upweighted ($\alpha_{NO_x} = 2$).

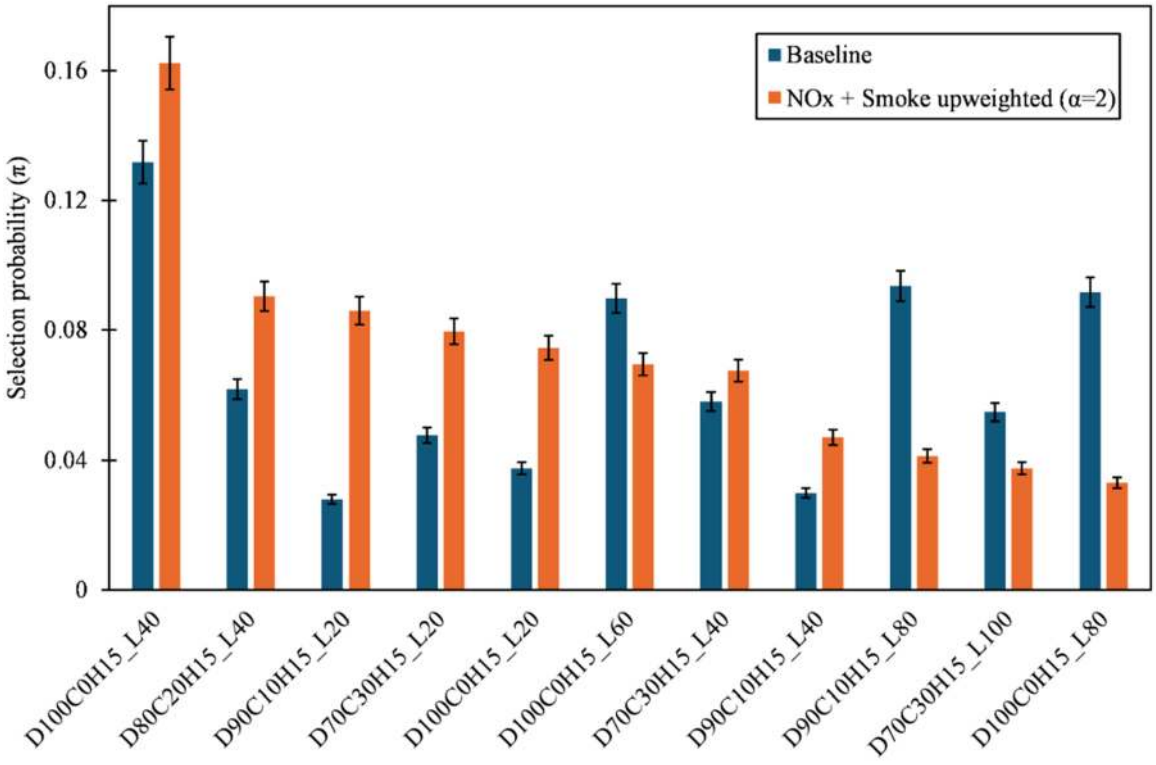


FIGURE 21 | Selection probabilities: baseline versus NO_x + Smoke upweighted ($\alpha_{NO_x} = 2$, $\alpha_{Smoke} = 2$).

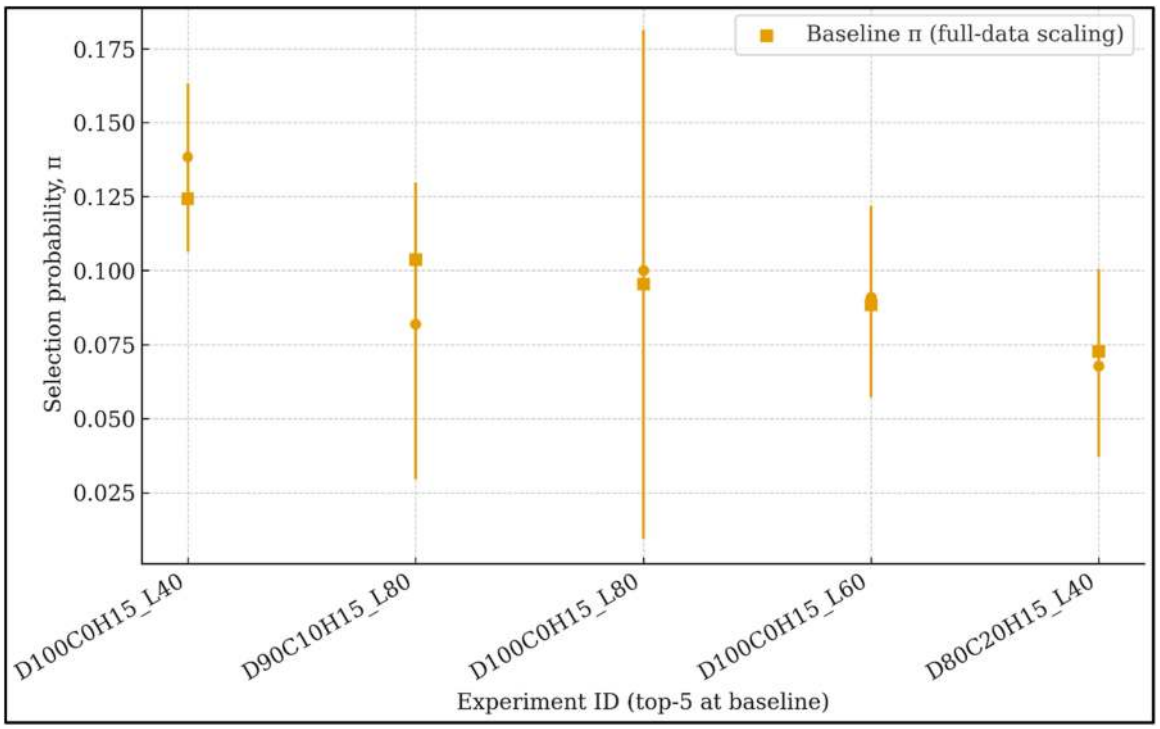


FIGURE 22 | Bootstrap stability of selection probability (Dirichlet $\alpha = 1$) under normalization uncertainty.

Together with the α-sweep (Figure 18) and policy scenarios (Figures 20 and 21), these bootstrap bands indicate that conclusions are decision grade. The preferred setting (D100C0H15_L40) remains the most likely choice under both preference and scaling uncertainty, while the calibration knobs needed to elevate near ties [45].

3.12.6 | *Dominance Gaps and HV*

Figure 23 decomposes the L_1 distance to the Pareto surface for the 10 closest nonwinners (i.e., dominated points with the smallest gaps). Three patterns are evident as follows:

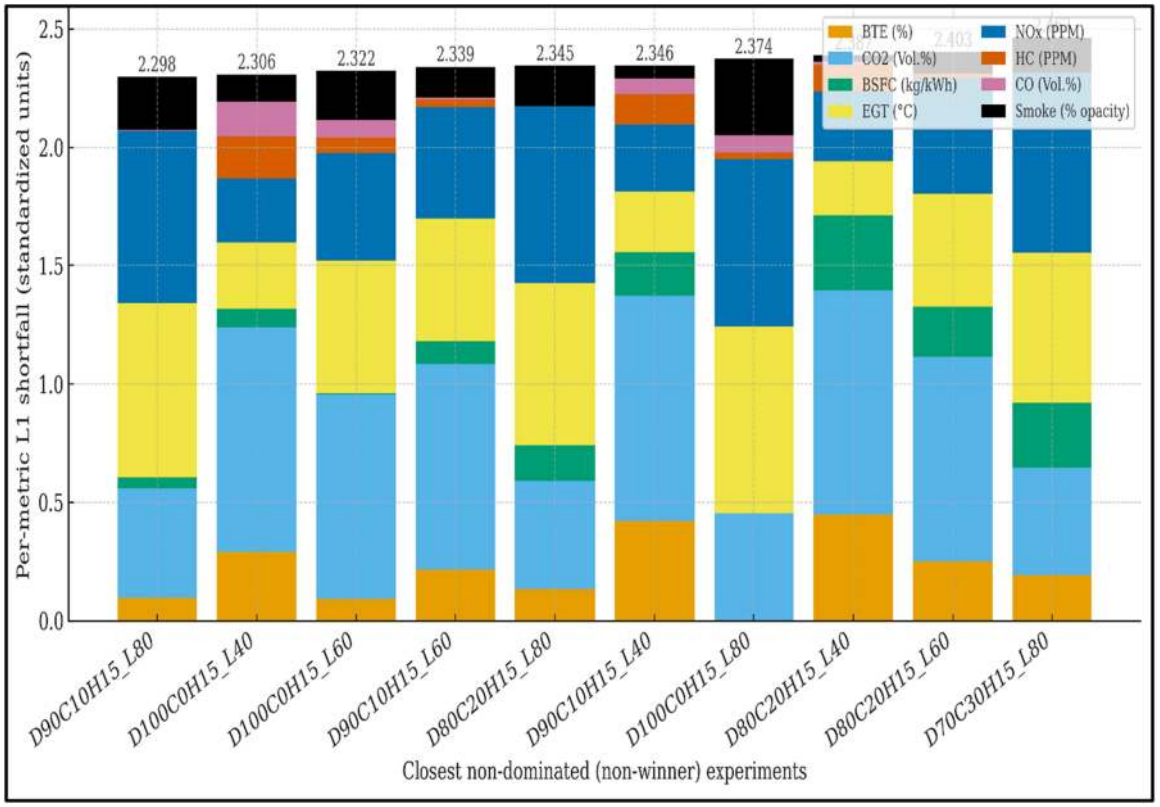


FIGURE 23 | Dominance-gap decomposition by metric (stacked L_1 contributions). BSFC, brake specific fuel consumption; BTE, brake thermal efficiency; EGT, exhaust gas temperature.

1. High-load H_2 cases fall short mainly on NO_x and, secondarily, BSFC, even when BTE and smoke scores are strong, for example, D100C0H15_L80 shows a total gap dominated by the largest ΔNO_x slice with a smaller ΔBSFC slice.
2. Biodiesel-only midloads trail on BTE and BSFC, not on smoke; the ΔSmoke slice is small, confirming oxygenation benefits.
3. Low-load entries are penalized by CO/HC (incomplete combustion) alongside BSFC; their ΔCO and ΔHC slices are visibly larger than other slices.

In the top-10 nonwinners, the median proportion of the gap to NO_x + BSFC is 58%–65% and the proportion of smoke is 8%–14%, which are consistent with Sections 3.6 and 3.10 trade-off narrative results. A calibration effort aimed at NO_x (e.g., small timing retard/or light EGR) should be made to increase near ties onto the front. To achieve lower BSFC on neat biodiesel points, the high-load H_2 cluster and fuel phasing/injection retuning should be used. The contribution of ΔSmoke to these blends is small and reducing smoke alone will have diminishing returns.

In $[0,1]^8$ standardized space, with the origin as the reference, Monte Carlo HV of the 10 best selections at each preference prior (3 repeats × 120k samples) are, Baseline ($\alpha = 1$): HV = 0.05505 ± 0.00050, NO_x upweighted ($\alpha_{NO_x} = 2$): HV = 0.05447 ± 0.00032, and NO_x + Smoke upweighted ($\alpha_{NO_x} = 2$, $\alpha_{Smoke} = 2$): HV = 0.05093 ± 0.00063. This set of desired results is the largest possible joint volume of desirable results, and NO_x (and NO_x + Smoke in particular) upweighting moves the selection to the cleaner corners, reducing overall HV by 1%–8%. This decrease is congruent with the policy, that is, with the focus on emissions, the viable utility mass is reduced, but the variety of solutions does not collapse diversity [46].

3.12.7 | *Confirmatory Runs (Decision Reproducibility)*

Decision reproducibility was assessed for the preference-agnostic selector by re-evaluating the baseline best setting and two near ties under three independent checks: (i) Monte Carlo binomial uncertainty of the selection probability π (Dirichlet $\alpha = 1$, $R = 20{,}000$), (ii) normalization uncertainty via bootstrap re-estimation of the 5%–95% quantiles ($B = 60$ resamples; $R = 2000$ utility draws per resample), and (iii) preference uncertainty via an α-sweep $\{0.25, 0.5, 1, 2, 4\}$. "Decision reproducible" is declared when (a) the baseline π lies within the bootstrap 95% band and (b) the configuration remains in the top-3 in at least 70% of bootstrap resamples.

The leading configuration D100C0H15_L40 shows high reproducibility, with baseline π enclosed by its bootstrap band and rank preserved in ≥ 70% of resamples (Table 6). The two near ties also meet the inclusion of π within bands, with rank preservation fractions indicating practical, though slightly lower, stability [43]. Across preference scenarios, the π of each top-3 configuration is varied within the reported $[\pi_{min}, \pi_{max}]$ range, confirming that moderate shifts in decision weights do not overturn the qualitative ordering.

The best and near ties reproduce under resampling-based perturbations of scaling and preferences. Consequently, the selection can proceed to physical confirmation (repeat engine trials)

TABLE 6 | Confirmatory runs and decision reproducibility (top-3 at baseline).

Blend	π _baseline	π _Wilson_low	π _Wilson_high	π _boot_mean	π _boot_low95	π _boot_high95	π _alpha_min.	π _alpha_max.	Rank_preservation	Reproducible
D100C0H15_L40	0.135	0.131	0.140	0.138	0.111	0.166	0.061	0.223	1.00	Yes
D90C10H15_L80	0.096	0.093	0.101	0.085	0.024	0.157	0.059	0.227	0.42	No
D100C0H15_L80	0.093	0.090	0.098	0.087	0.001	0.178	0.084	0.097	0.57	Borderline

with a narrow verification brief. $H_2 = 15\ L{\cdot}min^{-1}$ at 40% load (best) was maintained, and the two near ties were retested under identical boundary conditions to close the loop.

3.12.8 | *Mechanistic Interpretation of the Trade-off Structure*

The multiobjective trade-offs in this study are based on combined combustion pathways during operation of H_2-assisted, oxygenated fuel direct injection on the H_2 direct injection operation. Generally, a shift toward greater efficiency (greater BTE/smaller BSFC) is likely to raise the effective burned gas temperature and the premixed heat release fraction, which may increase thermal NO_x formation. On the other hand, the strategies that minimize NO_x are often based on the inhibition of peak temperatures and/or a delay in the effective combustion phasing, and this may carry an effectiveness penalty. Parallel to these, the inherent oxygen content of the biodiesel fraction helps in the reduction of smoke as well as enhancing soot oxidation and suppressing the growth of diffusion flames soot. Moreover, enrichment of the H_2 lowers the carbon content of the reacting blend and speeds up the oxidation reaction. Nonetheless, the H_2 facilitated rise in flame velocity and adiabatic temperature is able to increase the NO_x danger margin when the operating point is sidelined to higher load or higher substitution. This forms a limited clean efficiency band, in which soot may be suppressed, without causing an untenable NO_x increment, as long as the operating point is chosen not only under realistic preference trade-offs but also under one fixed weighting.

Low-load conditions are disproportionately penalized by incomplete combustion indicators (CO/HC) and higher BSFC because bulk gas temperatures and oxidation rates are weaker, and wall-quench effects become more prominent. Midload conditions provide sufficient thermal and turbulent mixing intensity to explore H_2 as a reactivity lever while retaining the soot suppression advantage of the oxygenated biodiesel fraction. High-load H_2-enriched points can deliver strong smoke suppression, but the incremental efficiency gains are offset by a steep NO_x rise. Therefore, these points only become competitive under extreme smoke-centric preferences, not under balanced multipollutant decision criteria.

3.13 | Benchmarking Results of SMAA

SMAA was explicitly designed for MCDM problems where criterion weights are incomplete, imprecise, or preference uncertain. SMAA complements deterministic ranking by estimating the Rank 1 acceptability, the probability of being in the *top-k* set, and the expected rank. This quantifies robustness among space uncertainty rather than relying on a single fixed weight vector.

3.13.1 | *Rank Acceptability Under Baseline Weight Uncertainty*

Under the baseline Dirichlet prior ($\alpha = 1$), the configuration D100C0H15_L40 exhibited the highest Rank 1 acceptability ($P(\text{best}) = 0.1353$) and a comparatively strong expected rank ($\mathbb{E}\text{rank}_1 = 14.03$), indicating that it is the most frequent winner across randomly sampled preference structures (Table 7).

TABLE 7 | SMAA benchmarking (baseline Dirichlet $\alpha = 1$): top-5 alternatives.

Configuration	P (*best*)	P (*top*-3)	P (*top*-5)	$\mathbb{E}$*rank*
D100C0H15_L40	0.135	0.235	0.312	14.03
D90C10H15_L80	0.097	0.255	0.374	17.51
D100C0H15_L80	0.094	0.217	0.307	20.39
D100C0H15_L60	0.093	0.215	0.303	16.49
D80C20H15_L40	0.064	0.203	0.311	16.39

Abbreviations: SMAA, Stochastic Multicriteria Acceptability Analysis.

Importantly, the probability mass is not concentrated on a single option, where the top-3 alternatives account for 0.3255 of Rank 1 acceptability, while the top-5 account for 0.4822. This demonstrates meaningful competition among a small set of near-optimal candidates when stakeholder trade-offs vary. Such rank dispersion is precisely the scenario where deterministic methods can be brittle, and where SMAA is recommended to quantify stability and rank disagreement risk [47]. Figure 24 summarizes the SMAA Rank 1 acceptability (P(best)) for the leading configurations under the baseline Dirichlet prior and the emissions prior (NO_x and NO_x + Smoke). This is used to assess winner stability and probability mass redistribution under the considered preference perturbations.

3.13.2 | *Sensitivity Benchmarking via Policy Tilted Weight Priors*

To test whether the ranking is robust to policy tilted preferences, two test priors were evaluated: NO_x upweighted and NO_x + Smoke upweighted. Under NO_x upweighting, D100C0H15_L40 remained the most acceptable winner and strengthened its dominance (P(best) increased from 0.1353 to 0.1883; $\mathbb{E}$rank improved from 14.03 to 11.53), indicating that the BEMORS optimum is not an artifact of a particular weight setting (Table 8). Under the NO_x + Smoke test, D100C0H15_L40 remained Rank 1 (P(best) = 0.1650 and $\mathbb{E}$rank = 10.56), while D80C20H15_L40 and D90C10H15_L20 shifted into the leading set, revealing the specific trade-off regime in which biodiesel fraction and loading conditions become competitive (Table 9). This aligns with the broader SMAA literature in which probability-of-best and expected rank are used to characterize shifts in the leading sample set under provided preference combinations, avoiding reliance on a single and potentially brittle ordering [48].

3.13.3 | *Cross-Scenario Stability of Leading Candidates*

Table 10 consolidates the Rank 1 acceptability and expected rank for the union of top samples across scenarios. D100C0H15_L40 is the only alternative that remains Rank 1 across all priors, with consistently improving expected rank as emissions criteria are prioritized ($\mathbb{E}$rank = 14.03–11.53–10.56). Structured rank shifts when Smoke is coprioritized, alternatives such as D80C20H15_L40 gain material probability mass (P(best) = 0.0961) and a strongly competitive expected rank ($\mathbb{E}$rank = 10.62). This is evidence of a traceable trade-off mechanism rather than arbitrary ranking instability, the type of interpretability SMAA is used to provide in stochastic benchmarking [47].

3.13.4 | *Central Weight Vectors for Interpretability*

To avoid reporting SMAA as a black box, the central weight vector associated with the best configuration (D100C0H15_L40) can be summarized (Table 11) to show the preference profile under which it is most representative. As expected, NO_x upweighting increased the central NO_x weight (0.183–0.250), while NO_x + Smoke upweighting increased the Smoke weight (0.111–0.166), with BTE and BSFC weights remaining in a similar band. This indicates that the best sample is not produced by an extreme, singular preference corner but by a broad, interpretable region of the weight space [19, 48].

4 | Limitations of the Study

The following are the limitations of this study:

- The engine was evaluated at a single fixed speed and at stabilized steady-state load points. Therefore, the results are directly applicable to steady-state conditions only.
- The experiments were conducted without exhaust aftertreatment (e.g., DPF/SCR). Therefore, the reported emissions represent engine-out levels, and tailpipe compliance implications cannot be inferred without aftertreatment integrated validation.
- The H_2 introduction architecture (manifold induction) was not cross-compared against port or direct induction, which can alter mixing, ignition delay, and NO_x formation windows.
- BEMORS uses 5%–95% percentile scaling to [0, 1], direction unification, and a Dirichlet prior for preference weights. These assumptions are reasonable but not unique: quantile scaling may compress extremes, Dirichlet weights may not represent all utility profiles, and Monte Carlo estimates introduce sampling errors.
- CO_2 vol% is used purely as a local combustion completeness indicator. Life cycle carbon performance depends on the fuel and H_2 production pathways and is not optimized in this study.
- The analysis was restricted to tank-to-wheel performance. The sustainable development goals (SDG) 7 benefits assume low carbon or renewable H_2 supply. If H_2 is produced from unabated fossil pathways, the improvements in local air quality and engine energy efficiency would remain, but life-cycle greenhouse gas reductions would be more modest.

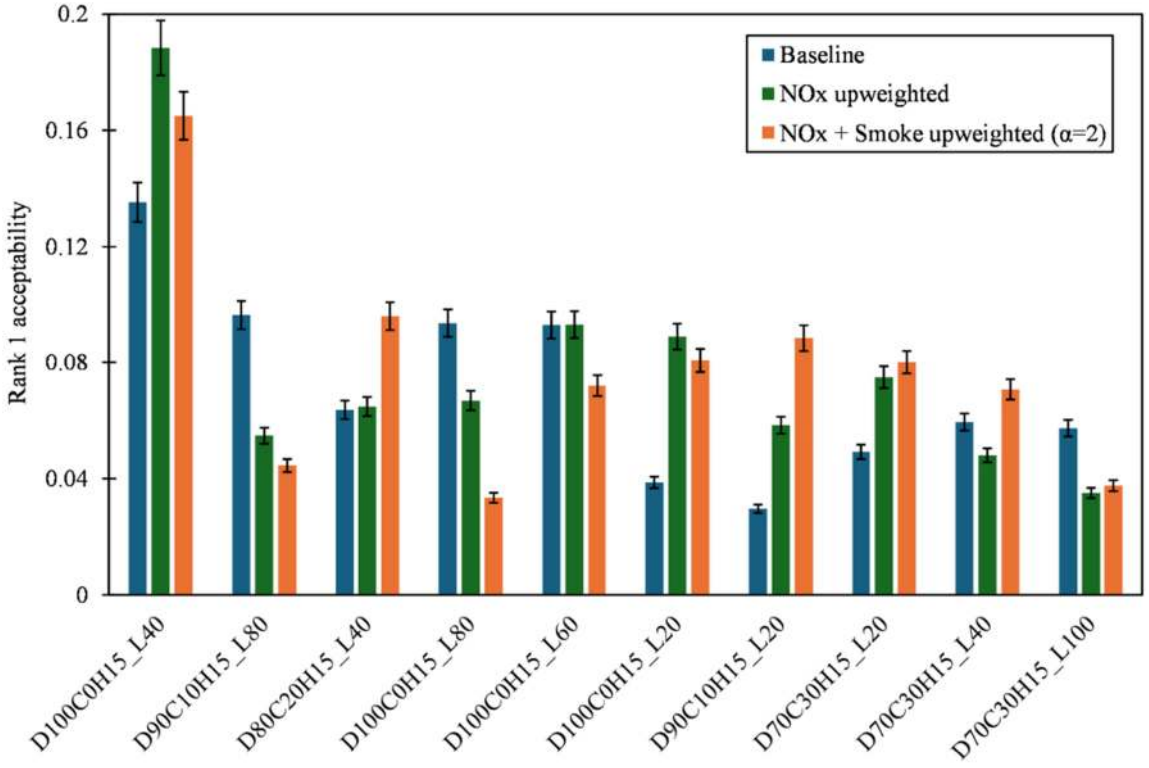


FIGURE 24 | Rank 1 acceptability bar plot for the top-10 alternatives under the three priors.

TABLE 8 | SMAA benchmarking (NO_x upweighted prior): top-5 alternatives.

Configuration	*P* (*best*)	*P* (*top*-3)	*P* (*top*-5)	$\mathbb{E}$*rank*
D100C0H15_L40	0.1883	0.3145	0.4071	11.53
D100C0H15_L60	0.0932	0.2182	0.2973	19.02
D100C0H15_L20	0.0891	0.1828	0.2686	22.08
D70C30H15_L20	0.0749	0.147	0.2115	30.42
D100C0H15_L80	0.0669	0.1581	0.2228	28.72

Abbreviations: SMAA, Stochastic Multicriteria Acceptability Analysis.

TABLE 9 | SMAA benchmarking (NO_x + Smoke upweighted prior): top-5 alternatives.

Configuration	*P* (*best*)	*P* (*top*-3)	*P* (*top*-5)	$\mathbb{E}$*rank*
D100C0H15_L40	0.165	0.2872	0.3902	10.56
D80C20H15_L40	0.0961	0.2791	0.4496	10.62
D90C10H15_L20	0.0886	0.2666	0.395	16.72
D100C0H15_L20	0.0808	0.1871	0.286	17.73
D70C30H15_L20	0.0801	0.1779	0.2603	23.79

Abbreviations: SMAA, Stochastic Multicriteria Acceptability Analysis.

- The preferred operating corridors identified in this study should be viewed as baseline guidance that must be validated under representative transient cycles.
- SMAA is not fully independent because it shares the same experimental criteria matrix, percentile scaling, and directionality mapping used for comparability with BEMORS. Therefore, SMAA is interpreted as a methodological sensitivity check on preference uncertainty (weight sampling) rather than a validation of combustion physics.

5 | Practical Implications

The findings of this study have several practical implications for deploying tri-fuel operations in existing diesel fleets. The results

TABLE 10 | Consolidated stability view (P(best)/$\mathbb{E}$rank) across scenarios.

Configuration	P(best) (Base)	$\mathbb{E}$rank (Base)	P(best) (NO_x)	$\mathbb{E}$rank (NO_x)	P(best) (NO_x + Smoke)	$\mathbb{E}$rank (NO_x + Smoke)
D100C0H15_L20	0.0387	30.19	0.0891	22.08	0.0808	17.73
D100C0H15_L40	0.1353	14.03	0.1883	11.53	0.1650	10.56
D100C0H15_L60	0.0931	16.49	0.0932	19.02	0.0720	19.38
D100C0H15_L80	0.0937	20.39	0.0669	28.72	—	—
D70C30H15_L20	0.0493	37.47	0.0749	30.42	0.0801	23.79
D80C20H15_L40	0.0636	16.39	0.0648	14.30	0.0961	10.62
D90C10H15_L20	—	—	0.0584	22.24	0.0886	16.72
D90C10H15_L80	0.0965	17.51	0.0548	26.61	0.0445	26.42

TABLE 11 | Central weight vector for D100C0H15_L40.

Scenario	w_{BTE}	w_{BSFC}	w_{NO_x}	w_{Smoke}	w_{CO}	w_{CO_2}	w_{EGT}	w_{HC}
Baseline	0.13	0.183	0.183	0.111	0.073	0.073	0.162	0.085
NO_x upweighted	0.128	0.167	0.25	0.098	0.074	0.075	0.118	0.091
NO_x + Smoke upweighted	0.129	0.167	0.226	0.166	0.065	0.069	0.1	0.079

Abbreviations: BSFC, brake specific fuel consumption; BTE, brake thermal efficiency; EGT, exhaust gas temperature.

show that meaningful efficiency gains are achievable with retrofit-level changes only. Hydrogen induction through the intake and on-board preparation of diesel–CIB blends is compatible with conventional single-cylinder engines. In the tested configuration, diesel supplemented with 15 $L \cdot min^{-1}$ H_2 at 40%–60% load increased BTE by about 8%–14% and reduced BSFC by 13%–17%, identifying a realistic mid-load operating window where more shaft work is obtained per unit fuel. The tri-fuel policy provides physical air quality in the small and medium duty cycles. CO, HC, and smoke are severely suppressed by hydrogen and CIB at high load, usually by 50%–70%, even during periods of NO*x* increase, thus the method is appealing in rural and semi-urban conditions where opacity and HC are the major factors of concern. The linear increase in NO_x is, however, an indication that field deployment would have to be integrated with traditional mitigation methods (e.g., mild injection retard, EGR, or aftertreatment). From an SDG 7 perspective, the optimized tri-fuel settings increase the contribution of nonedible CIB in the overall fuel energy supply while maintaining stable operation, thereby raising the renewable and clean fuel share in delivered shaft power (Target 7.2). At the same time, the observed increases in BTE and reductions in BSFC translate into a lower energy intensity of work output, consistent with Target 7.3, with emphasis on improved energy efficiency. Because the proposed configuration can be implemented as a retrofit on widely deployed agricultural and stationary diesel engines with limited hardware changes, it provides a practical pathway for delivering cleaner, more efficient energy services in constrained settings of resources, in line with the 'affordable, reliable and modern energy' framing of Target 7.1. Future work should extend these settings to transient duty cycles and integrate EGR/SCR calibration within the BEMORS loop.

6 | Conclusions

This study experimentally evaluated diesel–CIB–H_2 operation on Kirloskar TV1 single-cylinder direct injection engine operated at 1500 rpm under stabilized steady-state loads (20%–100%), using manifold H_2 induction (0–15 $L \cdot min^{-1}$) and CIB blends (0–30 vol%). A bootstrapped, empirical multi-objective ranking and selection methodology was applied to identify settings that balance efficiency and multipollutant outcomes without committing to a single set of weights. The combined experimental results provided decision-oriented guidance within the tested operating envelope and under explicitly defined preference scenarios. The following are the key findings of this study:

- Improvements that exceeded the combined uncertainty threshold (3.3%) were emphasized as robust outcomes, whereas small differences within this margin were interpreted as marginal variations.
- Hydrogen enrichment increased BTE across loads for neat diesel (e.g., +8%–14% at 40%–60% load; up to +8% at full load), while BSFC decreased correspondingly (13%–17% at $\geq$ 60% load). Biodiesel alone reduced BTE, but H_2 partly recovered it. At 30% biodiesel, $H_2 = 15\ L \cdot min^{-1}$ restored BTE by 20% relative to the biodiesel-only case.
- EGT increased monotonically with load. H_2 increased EGT for neat diesel, whereas CIB tended to lower EGT at similar load, with nonmonotonic responses at high biodiesel shares.
- Hydrogen injection sharply reduced CO/HC and smoke (50%–68% at high load), and biodiesel further suppressed smoke. However, NO_x increased with H_2 dose and modestly with biodiesel share. CO_2 volume fraction decreased

slightly with H_2 substitution, consistent with reduced carbon flow to the cylinder for a given delivered energy.

- Within the tested envelope, the decision analysis indicates that efficiency with low opacity, the decision method selects to operate at 40%–60% load with H_2 of 15 $L \cdot min^{-1}$ on neat diesel. If smoke limits tighten, H_2 with 20% CIB at 40% load is recommended.
- Under Dirichlet ($\alpha = 1$), BEMORS identified D100C0H15 at 40% load emerged as the best combination. Bootstrap bands on selection probability and α-sweeps confirmed ranking robustness.
- Policy-weighted priorities (NO_x or NO_x + Smoke up-weighting) shifted mass toward midload, H_2-assisted settings, and (for NO_x + Smoke) toward moderate biodiesel shares, with only modest HV loss.
- Benchmarking the proposed BEMORS decision method against SMAA confirmed that the leading operating point remains a highly acceptable solution across baseline and emissions tilted priorities.
- The efficiency-NO_x trade-off is consistent with higher premixed heat release/temperature with increased H_2 energy share, whereas smoke and CO/HC reductions align with improved oxidation and reduced carbon intensity.

Overall, the results demonstrated that H_2 supplementation, optionally paired with CIB, can deliver materially higher efficiency and far lower soot/CO/HC, with NO_x trade-off. This study can extend the experimental investigation to multiple engine speeds and transient duty cycles (load/speed sweep or representative cycle segments) and report mass-specific emissions ($g \cdot kWh^{-1}$) alongside concentration metrics. Also, evaluate alternative H_2 delivery strategies (port injection and/or direct injection) and integrate aftertreatment constraints (e.g., DPF/SCR and relevant NO_x-soot windows) within the BEMORS/SMAA decision method. This enables a calibrated optimization of efficiency-NO_x-smoke trade-off under engine-out and tailpipe-oriented objectives.

Funding

The authors received no specific funding for this work.

Conflicts of Interest

The authors declare no conflicts of interest.

Data Availability Statement

The data used for the research described in the article are within the article/Supporting Information.

References

1. B. Birhanu, D. Deshmukh, and K. Yeneneh, "*Podocarpus falcatus* as a Next-Generation Biodiesel Feedstock: Comparative Insights With *Jatropha curcas* on Oil Yield, Production, Properties, and Spray Behavior," *Discover Applied Sciences* 8 (2026): 246, https://doi.org/10.1007/s42452-026-08282-0.

2. K. Yeneneh and G. Sufe, "Sustainable Biodiesel Production From Cottonseed Oil Using a Nickel-Doped Eggshell Heterogeneous Catalyst Optimized via Response Surface Methodology," *Scientific Reports* 15, no. 1 (2025): 32132, https://doi.org/10.1038/s41598-025-17529-6.

3. B. Birhanu, D. Deshmukh, T. Hailelule, and K. Yeneneh, "RSM-Optimized Biodiesel Production From Ethiopian *Podocarpus falcatus* Seed Oil Using a CaO—CeO_2 Heterogeneous Composite Catalyst and Oxidative Stability Assessment," *Scientific Reports* 16 (2025): 3919, https://doi.org/10.1038/s41598-025-34007-1.

4. N. Kumar, D. Kumar, and A. Mishra, "A Study on Hydrogen Supplementation in a Compression Ignition Engine Fuelled With Diesel/Biodiesel Mixtures: Efficiency and Emission Trade-Offs," *Cleaner Chemical Engineering* 12 (2025): 100207, https://doi.org/10.1016/j.clce.2025.100207.

5. C. Selvam, Y. Devarajan, A. K. Dash, et al., "Improving Diesel Engine Performance With Hydrogen-Fumigated Soapnut Biodiesel," *Results in Engineering* 27 (2025): 106287, https://doi.org/10.1016/j.rineng.2025.106287.

6. U. Paneerselvam and K. Ganapathy, "Effect of Hydrogen Induction on CI Engine Characteristics Fuelled With Kapok Oil Methyl Ester-Turpentine Blend With Diethyl Ether," *Biofuels* 16, no. 4 (2025): 389–405, https://doi.org/10.1080/17597269.2024.2431390.

7. K. Ramalingam, M. Z. Abdullah, P. V. Elumalai, et al., "Production and Utilization of Hydrogen Enriched Fifth Generation Biofuel in LTC Engines With Reformed EGR," *Scientific Reports* 15, no. 1 (2025): 25922, https://doi.org/10.1038/s41598-025-08259-w.

8. M. Srinivasarao, C. Srinivasarao, A. S. Kumari, et al., "Combustion Enhancement and Emission Reduction in an IC Engine by Adopting ZnO Nanoparticles With *Calophyllum* Biodiesel/Diesel/Propanol Blend: A Case Study of General Regression Neural Network (GRNN) Modelling," *Industrial Crops and Products* 227 (2025): 120812, https://doi.org/10.1016/j.indcrop.2025.120812.

9. M. Anish, P. Bency, J. Jayaprabakar, et al., "An Evaluation of Biosynthesized Nanoparticles in Biodiesel as an Enhancement of a VCR Diesel Engine," *Fuel* 328 (2022): 125299, https://doi.org/10.1016/j.fuel.2022.125299.

10. P. Prasannakumar, R. Santhakumari, A. D. Thampi, E. Sneha, K. S. Adithyan, and S. Sabarinath, "Epoxidation of *Calophyllum inophyllum* Oil Fatty Acid Methyl Esters as a Potential Base-Stock for Green Cutting Fluid," *Environment, Development and Sustainability* 28 (2024): 973–997, https://doi.org/10.1007/s10668-024-05018-1.

11. A. S. Kurhade, P. S. Bhambare, S. Y. Waware, R. Biradar, R. S. Yadav, and V. N. Patil, "A Comprehensive Study on *Calophyllum inophyllum* Biodiesel and Dimethyl Carbonate Blends: Performance Optimization and Emission Control in Diesel Engines," *Journal of Mines, Metals & Fuels* 72, no. 5 (2024): 499–507, https://doi.org/10.18311/jmmf/2024/45188.

12. M. A. Prasanth, S. Rani, S. P. Singh, D. E. Raja, and P. Barmavatu, "Formulation and Evaluation of Bio-Grease From the Blend of Chemically Modified Rice Bran Oil and *Calophyllum inophyllum* Oil," *Journal of Engineering and Applied Science* 71, no. 1 (2024): 80, https://doi.org/10.1186/s44147-024-00414-w.

13. S. Vellaiyan, "Optimization of Hydrogen-Enriched Biodiesel–Diesel Dual-Fuel Combustion With EGR for Sustainable Engine Performance," *International Journal of Hydrogen Energy* 128 (2025): 85–94, https://doi.org/10.1016/j.ijhydene.2025.04.239.

14. Y. Devarajan and T. Raja, "Characterization of Isopropanol-Enhanced Caesalpinia Bonduc Biodiesel Blends: A Sustainable Strategy for Decarbonization," *Results in Engineering* 25 (2025): 103849, https://doi.org/10.1016/j.rineng.2024.103849.

15. W. Zhang, J. Ou, Z. Chen, Z. Li, L. Zhijun, and M. Pan, "Multi-Objective Performance Optimization of Diesel Engine Lip Jet Combustion Chamber Based on RSM-NSGA-II," *Energy* 330 (2025): 136825, https://doi.org/10.1016/j.energy.2025.136825.

16. A. Dong, L. Liu, C. Zhao, and Y. Guan, "Neural Network Prediction of Locomotive Engine Parameters Based on the Dung Beetle Optimization Algorithm and Multi-Objective Optimization of Engine Operating Parameters," *Sensors* 25, no. 3 (2025): 677, https://doi.org/10.3390/s25030677.

17. M. Nian, R. Dong, W. Zhong, Y. Zhang, and D. Lou, "Multi-Objective Optimization Study on Capture Performance of Diesel Particulate Filter Based on the GRA-MLR-WOA Hybrid Method," *Sustainability* 17, no. 19 (2025): 8777, https://doi.org/10.3390/su17198777.

18. L. C. Dias, "On the Sigma-Mu Stochastic Multicriteria Analysis: Exact Solutions for Common Particular Cases," *Omega* 127 (2024): 103093, https://doi.org/10.1016/j.omega.2024.103093.

19. Z. Xu, P. Liu, P. Li, and C. Wei, "A Stochastic Multi-Criteria Acceptability Analysis-Based Group Consensus Model Considering Overlapping Decision-Makers," *Engineering Applications of Artificial Intelligence* 159 (2025): 111782, https://doi.org/10.1016/j.engappai.2025.111782.

20. R. K. Gaur and R. Goyal, "Performance, Emission, Combustion and Economics Analysis of CI Engine Fueled With Mixed Oil Biodiesel Blends From Waste Cooking Oil and Pongamia Oil," *Discover Applied Sciences* 7, no. 6 (2025): 609, https://doi.org/10.1007/s42452-025-07150-7.

21. H. Yıldırım, A. N. Özsezen, A. Çınar, T. Kaya, and S. Karabay, "Effects of Rail Pressure on the Combustion and Vibro-Acoustic Characteristics of a Diesel Engine Running on Biodiesel," *Arabian Journal for Science and Engineering* 51 (2025): 3255–3270, https://doi.org/10.1007/s13369-025-10241-7.

22. M. Anish, J. R. Deepak, J. Giri, et al., "Enhancing Compression Ignition Engine Efficiency and Reducing Noise Emissions: The Impact of Nanoparticle Enhanced Biodiesel Blends," *Ain Shams Engineering Journal* 16, no. 10 (2025): 103507, https://doi.org/10.1016/j.asej.2025.103507.

23. B. Singh, A. K. Srivastava, and O. Prakash, "Effect on Combustion Performance and Emission Behavior of Diesel Engine Fueled With Hybrid Biodiesel Produced From a Novel Ternary Oil Mixture Incorporated With Nano Additive," *Energy Sources, Part A: Recovery, Utilization, and Environmental Effects* 46, no. 1 (2024): 6566–6585, https://doi.org/10.1080/15567036.2024.2351149.

24. M. U. S. Akhtar, F. Asfand, A. S. Mishamandani, R. Mishra, and M. I. Khan, "Hydrogen as a Sustainable Combustion Fuel: Performance, Challenges, and Pathways for Transition to Low-Carbon Propulsion Systems," *Renewable and Sustainable Energy Reviews* 223 (2025): 116004, https://doi.org/10.1016/j.rser.2025.116004.

25. C. Reitmayr and P. Hofmann, "Strategies to Increase Hydrogen Energy Share of a Dual-Fuel Hydrogen–Kerosene Engine for Sustainable General Aviation," *Hydrogen* 6, no. 1 (2025): 17, https://doi.org/10.3390/hydrogen6010017.

26. K. Yeneneh, G. Sufe, and Z. J. Sroka, "Performance, Combustion, and Emission Characteristics of a Diesel Engine Fueled With Preheated Coffee Husk Oil Methyl Ester (CHOME) Biodiesel Blends," *Sustainability* 17, no. 19 (2025): 8678, https://doi.org/10.3390/su17198678.

27. Q. Zhang, Z. Li, Y. Xu, and X. Li, "Effects of Circumferential and Interaction Angles of Hydrogen Jets and Diesel Sprays on Combustion Characteristics in a Hydrogen–Diesel Dual-Fuel CI Engine," *Sustainability* 17, no. 13 (2025): 6059, https://doi.org/10.3390/su17136059.

28. B. Mehta, A. Swarnkar, and D. Subhedar, "Performance and Emission Evaluation of Diesel Engines Using Karanja Biodiesel Blended With Diethyl Carbonate," *Results in Engineering* 27 (2025): 106548, https://doi.org/10.1016/j.rineng.2025.106548.

29. E. Dimitrov, A. Tashev, M. Peychev, and E. Pavlova, "Methodologies for Conducting Experimental Studies Related to the Application of Gaseous Fuels in Internal Combustion Engines," *Journal of Physics: Conference Series* 3099, no. 1 (2025): 012004, https://doi.org/10.1088/1742-6596/3099/1/012004.

30. P. Bridjesh, P. Periyasamy, A. V. Krishna Chaitanya, and N. K. Geetha, "MEA and DEE as Additives on Diesel Engine Using Waste Plastic Oil Diesel Blends," *Sustainable Environment Research* 28, no. 3 (2018): 142–147, https://doi.org/10.1016/j.serj.2018.01.001.

31. V. Periyathambi, M. Ezhumalai, M. Govindasamy, R. Dhairiyasamy, D. Varshney, and S. Singh, "Balancing Efficiency and Emissions: A Study on Biodiesel–Hydrogen Dual-Fuel Engine Performance Under Varying Injection Timings," *Engineering Reports* 7, no. 5 (2025): e70174, https://doi.org/10.1002/eng2.70174.

32. S. Ellappan and B. Pappula, "Utilization of Unattended Waste Plastic Oil as Fuel in Low Heat Rejection Diesel Engine," *Sustainable Environment Research* 29, no. 1 (2019): 2, https://doi.org/10.1186/s42834-019-0006-7.

33. P. Bridjesh, N. Prabhu Kishore, M. V. Mallikarjuna, and N. Alekhya, "Performance Analysis of Variable Compression Ratio Diesel Engine Using *Calophyllum inophyllum* Biodiesel," *Indian Journal of Science and Technology* 9, no. 35 (2016): 1–5, https://doi.org/10.17485/ijst/2016/v9i35/95577.

34. S. Madhu, A. K. Chaitanya, and P. Bridjesh, "Effects of Diethyl Ether on Performance and Emission Characteristics of a Diesel Engine Using Toroidal Profile Bowl Piston by Varying Injection Pressure," *International Journal of Mechanical Engineering and Technology* 8, no. 6 (2017): 96–106.

35. N. K. Geetha and B. Pappula, "Integrated AHP and WED Based Approach to Select Optimal Combination of Operating Parameters on Spark Ignition Engine," *SAE Technical Paper* (2019), https://doi.org/10.4271/2019-01-0025.

36. G. N. Kannaiyan, B. Pappula, and S. Makgato, "Experimental Investigation on Addition of Furfuryl Alcohol to Diesel Plastic Fuel Blends and Optimization Using Kissing Numbers," *Scientific Reports* 15, no. 1 (2025): 20672, https://doi.org/10.1038/s41598-025-07174-4.

37. N. K. Geetha and P. Bridjesh, "Combinatorial Rough Neutrosophic Multi Attribute Decision Making Approach for Selection of Waste Plastic Oil–Diesel Blends," *Materials Today: Proceedings* 37 (2021): 979–981, https://doi.org/10.1016/j.matpr.2020.06.186.

38. M. Guan, J. Rochussen, P. Steiche, et al., "Characterizing Hydrogen–Diesel Dual-Fuel Performance and Emissions in a Commercial Heavy-Duty Diesel Truck," *International Journal of Hydrogen Energy* 86 (2024): 1085–1096, https://doi.org/10.1016/j.ijhydene.2024.08.480.

39. F. Ekin, O. A. Ozsoysal, and H. Arslan, "The Effect of Using Hydrogen at Partial Load in a Diesel–Natural Gas Dual Fuel Engine," *International Journal of Hydrogen Energy* 47, no. 42 (2022): 18532–18550, https://doi.org/10.1016/j.ijhydene.2022.03.287.

40. R. Pelissari, M. C. Oliveira, S. B. Amor, A. Kandakoglu, and A. L. Helleno, "SMAA Methods and Their Applications: A Literature Review and Future Research Directions," *Annals of Operations Research* 293, no. 2 (2020): 433–493, https://doi.org/10.1007/s10479-019-03151-z.

41. R. G. García-Cáceres, "Stochastic Multicriteria Acceptability Analysis–Matching (SMAA-M)," *Operations Research Perspectives* 7 (2020): 100145, https://doi.org/10.1016/j.orp.2020.100145.

42. S. Lakmayer and M. Danielson, "Efficient Weight Ranking in Multi-Criteria Decision Support Systems," *Electronics* 14, no. 7 (2025): 1237, https://doi.org/10.3390/electronics14071237.

43. L. De Santanna, R. Malacrida, G. Mastinu, and M. Gobbi, "An Application of Reinforcement Learning to the Optimal Design of Road Vehicle Suspension Systems," *Designs* 9, no. 5 (2025): 108, https://doi.org/10.3390/ai5040085.

44. S. Jiang and W. Zhang, "A Hybrid Approach of Modified Bootstrap and Physics-Based Methods for Probabilistic Fatigue Life Prediction

Considering Overload Effects," *Probabilistic Engineering Mechanics* 70 (2022): 103343, https://doi.org/10.1016/j.probengmech.2022.103343.

45. C. Audet, J. Bigeon, D. Cartier, S. Le Digabel, and L. Salomon, "Performance Indicators in Multiobjective Optimization," *European Journal of Operational Research* 292, no. 2 (2021): 397–422, https://doi.org/10.1016/j.ejor.2020.11.016.

46. A. P. Guerreiro, C. M. Fonseca, and L. Paquete, "The Hypervolume Indicator: Computational Problems and Algorithms," *ACM Computing Surveys* 54, no. 6 (2021): 1–42, https://doi.org/10.1145/3453474.

47. D. M. Mahalak, "A Simulation-Based Comparison of Deterministic and Stochastic Multicriteria Models: Analyzing Rank Divergence," *Journal of Multi-Criteria Decision Analysis* 32, no. 2 (2025): e70016, https://doi.org/10.1002/mcda.70016.

48. D. Zhang, F. Li, and L. Wei, "Integrated Stochastic Multicriteria Acceptability Analysis and Data Envelopment Analysis With Fixed-Sum Outputs: An Application for Evaluating Participating Nations in the Winter Olympics Games," *Journal of the Operational Research Society* 75, no. 9 (2024): 1791–1812, https://doi.org/10.1080/01605682.2023.2277251w.

Supporting Information

Additional supporting information can be found online in the Supporting Information section.

Table S1: Experimental matrix and measured responses for all 90 tests (inputs: Diesel, Calophyllum biodiesel, H_2, Load; outputs: BSFC, BTE, EGT, NO_x, HC, CO, CO_2, Smoke). **Table S2:** The inlet hydrogen energy fraction across test fuels at 20, 40, 60, 80, and 100% loads.